ATTENUATION TOMOGRAPHY OF SIERRA NEGRA VOLCANO

Rebecca Lynn Rodd

A Master's Thesis submitted to the faculty of the University of North Carolina at Chapel Hill in partial fulfillment of the requirements for the degree of Masters of Science in the Department of Geological Sciences.

Chapel Hill
2016

Approved by:

Jonathan M. Lees

Jose A. Rial

Cemal B. Biryol

ABSTRACT

Rebecca Lynn Rodd: Attenuation Tomography of Sierra Negra Volcano
(Under the direction of Jonathan M. Lees)

The first fine-scale image of the shallow magma system beneath Sierra Negra is determined using attenuation tomographic methods. The t^* spectral decay method for P-wave phases was used to highlight regions of high Q_p^{-1} which suggest the presence of magma melt. High Q_p^{-1} anomalies, ranging from $0.005 - 0.04$, are concentrated beneath the caldera from $0.5 - 10.5$ km depths. The high attenuation is interpreted as a zone of magma accumulation. Modeling of caldera deformation indicates a magma sill or flat-topped diapir at 2.1 km depth of unknown thickness. The attenuation model supports the diapir model.

To Kaity and Kuma

ACKNOWLEDGMENTS

I would like to thank my research advisor, Dr. Jonathan Lees for providing support, guidance and trust throughout the duration of this project. He also provided technical support with coding. I utilized his RCran packages, RSEIS and Rquake for seismic analysis and earthquake relocation. I would also like to thank my committee members, Dr. Jose Rial and Dr. Berk Biryol, who provided insight and support for this research.

The Department of Geological Sciences, in particular the Seismology Lab group, have provided me with ample support and kindness. When I came to UNC, Daniel Bowman was welcoming, kind and offered some of the best advice one could ask for. Jordan Bishop assisted in picking phase arrivals. This is an arduous task and I am very grateful for his assistance. Finally, I want to mention Sanja Knezevic Antonijevic , Elizabeth Reischmann and Tim Ronan who were always available for research discussion and advice.

Data for this research was collected by Instituto Geofisico Nacional Escuela Politecnica, University of Rochester, University of Miami, University of Idaho, and the Charles Darwin Foundation. Data and metadata for this deployment are available through the IRIS Data Management Center (DMC), network code XE. Gabrielle Tepp provided the P-wave body wave tomography model and initial ambient noise results. This research was supported by National Science Foundation (NSF) Grant CDI-Type II 1125185 and UNC Department of Geological Sciences' Martin Fund Grant.

TABLE OF CONTENTS

LIST OF TABLES

LIST OF FIGURES

CHAPTER 1.

Introduction

Sierra Negra is one of the most active volcanoes in the Galápagos Archipelago. Eruptions occur approximately every 15 years, but seismicity is a continuous feature during eruptive and non-eruptive periods. Local seismicity at Sierra Negra was recorded during two time periods, from 1999-2003 and 2009-2011. These data sets have been used to produce abundant geophysical studies on the Galápagos that have furthered our understanding of the subsurface structure beneath the islands and the formation and growth of hot-spot volcanism.

Geodetic modeling of deformation indicates a shallow magma reservoir that controls the deformation, faulting, and eruptive behavior of Sierra Negra. The scales of previous studies are too large to image such a feature. The target of this project is to image the subsurface beneath Sierra Negra using attenuation tomography to determine the geometry and thermal properties of the shallow magmatic system.

The following topics will be covered:

- Chapter 2: Brief review of geology and geophysics of Galápagos and Sierra Negra Volcano
- Chapter 3: Review of seismic attenuation and methodologies for measuring attenuation
- Chapter 4: Imaging the attenuation structure beneath Sierra Negra

CHAPTER 2.

Geologic Background

2.1 Galápagos Archipelago

The Galápagos Archipelago is a hotspot volcanic system consisting of 15 islands constructed on a large submarine platform. It is located on the Nazca ridge approximately 1000 km west of Ecuador and 200 km south of the Galápagos Spreading Center (GSC) (Figure 2.1). The Nazca ridge is migrating eastward perpendicular to the GSC spreading motion (Figure 2.2). Geochemical and geophysical evidence indicate that the archipelago has interacted with the GSC in the recent past.

2.1.1 Mantle Plume

The temporal and spatial correlation with eastward migration (i.e. younger in the west), He_3/He_4 isotopic signatures, and low-seismic velocity zone penetrating into the upper mantle [*Villagomez et al.*, 2007] suggest a mantle-plume beneath the archipelago. Hotspot-ridge interaction models predict that the plume deflects in the direction of plate motion and that transportation of plume material occurs near the base of the thermal lithosphere. Surface-wave tomography results reveal the plume, centered at 91° W, deflecting towards the GSC at depths $>$ 100 km, almost perpendicular to plate motion (Figure 2.3). As a result, the plume axis is further northwest than predicted for viscous coupling between plate motion and plume [*Villagomez et al.*, 2007, 2014]. *Villagomez et al.* [2014] attributes these observation to lack of viscous coupling between plume and plate motion.

Geochemical observations of the GSC indicate strong plume signatures, even greater than that of the archipelago. It is hypothesized that transport of plume material towards

the GSC occurs in the deeper asthenosphere resulting in the plume geochemical signature at 91° W on the GSC.

2.1.2 Lithosphere

The base of the lithosphere beneath the Galápagos is defined as the bottom of the high-velocity lid from surface-wave tomography [*Villagomez et al.*, 2007] and the top of the melt-column depth from geochemical modeling. Tomography results indicate variable lithosphere thickness, thicker ($\sim$ 70 km) in the west proximal to the plume axis (southwest of Fernandina Island and northwest of Isabella Island) and thinner ($\sim$ 40 km) in the east and north [*Villagomez et al.*, 2007]. Estimates from geochemical modeling corroborate these estimates [*Villagomez et al.*, 2007] with $\sim$ 60 and $\sim$ 45 km thickness in the west and east, respectively, and local lateral fluctuations up to 15 km [*Gibson and Geist*, 2010].

Although conductive cooling can explain an increase in thickness moving away from the GSC (i.e. older lithosphere is thicker), the thickness is greater than expected for a thermally-defined lithosphere. A dehydrated and iron depleted lithosphere with melt injection could explain the thicker lithosphere and slow seismic velocities [*Villagomez et al.*, 2007; *Gibson and Geist*, 2010; *Rychert et al.*, 2014]. Abrupt migration of the GSC southward could account for the heterogeneities in lithospheric thickness in the east, age discontinuities, and plume isotopic signatures of the GSC [*Gibson and Geist*, 2010].

Large gradients in lithospheric thickness may produce the observed compositional diversity of the Galápagos volcanoes. In the west, where lithosphere is thick but laterally homogeneous, volcanic deposits tend to be compositionally uniform with incompatible-trace element and depleted low-K tholeiitic basalts. In the east, where lithosphere is thin and laterally heterogeneous, volcanoes are compositionally diverse, ranging from depleted (MORB-like) to enriched [*Gibson and Geist*, 2010].

2.1.3 Mohorovicic Discontinuity

The depth of the Moho beneath the Galápagos Archipelago is still debated. Receiver function results identify a high-velocity increase at 11 ± 7 km depth [*Rychert et al.*, 2014]. However, body-wave tomography did not image an impedance boundary at this depth [*Tepp et al.*, 2014]. Another velocity increase was imaged at 37 km depth [*Rychert et al.*, 2014] consistent with surface wave tomography results [*Villagomez et al.*, 2007, 2014]. The current model suggests multiple impedance boundaries that are attributed to overplating and underplating of magmatic material on and/or beneath the pre-plume crust.

2.2 Sierra Negra

Sierra Negra is one of the most voluminous and active volcanoes in Galápagos Archipelago. It has a shallow, elliptical caldera (7 x 10 km) and sinuous ridge formed from near-vertical normal faults that run roughly parallel to the eastern and southern caldera [*Reynolds et al.*, 1995]. The shallow caldera and ridge feature are unique to Sierra Negra. On average, eruptions occur every 15 years and produce $1 \cdot 10^6 \frac{m^3}{yr}$ deposits [*Reynolds et al.*, 1995].

Observations and modeling from geodetic studies indicate the caldera floor has been actively deforming since at least 1992. The deformation is characterized by radial doming with occasional asymmetry due to faulting along the southern sinuous ridge. During 1997-1998, asymmetric deformation led to 1.5 ± 0.2 m displacement (Figure 2.4). Modeling suggests that episodic intrusions from a deep source pressurizes a flat-topped magma sill or diapir at 2.1 km depth, causing domed inflation, trapdoor faulting, and often magma extrusion [*Amelung et al.*, 2000; *Jonsson et al.*, 2005; *Yun et al.*, 2006; *Chadwick et al.*, 2006; *Geist et al.*, 2008]. The geometry of the top of the diapir is the same as the sill. Results indicate that the lower extent of the reservoir does not control deformation. As a result, the dimension and geometry of the reservoir are unknown. Understanding the geometry of this reservoir would shed light on potential eruptive volumes and locations

of surface rupture.

During the most recent 2005 eruption, deflation occurred due to the extrusion of $150 \cdot 10^6$ m^3 volume of magma from the shallow reservoir followed by re inflation after the eruption [*Geist et al.*, 2008]. Ongoing inflation in conjunction with high caldera seismicity, including evidence of magma intrusion south of the caldera recorded as recently as 2011 [*Tepp et al.*, 2014], indicate that the shallow magma reservoir and deeper source is a persistent feature.

Travel-time tomography identified a patchwork of high- and low- V_p anomalies beneath Southern Isabela Island (Figure 2.5) . These results were best reconstructed by a 15 km diameter low V_p region with superimposed volumetrically smaller, lower V_p anomalies. This body is interpreted as a 15 km wide zone of magma accumulation beneath the caldera from $5.5 - 15$ km depth. The V_p model could not resolve features above 3 km depth, such as the proposed shallow reservoir [*Tepp et al.*, 2014].

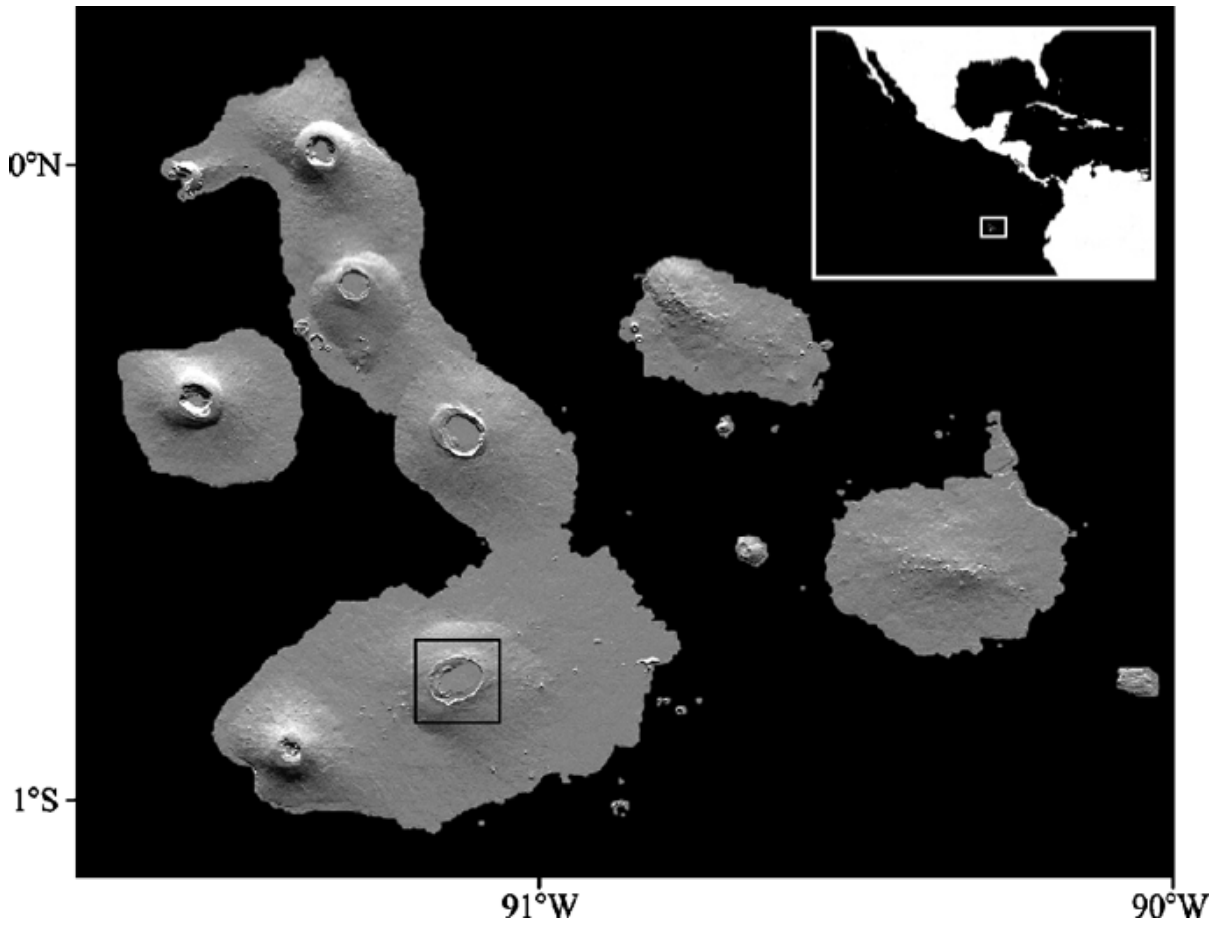

Figure 2.1: Reference map of Galápagos Islands relative to South America. Image is from *Yun et al.* [2006].

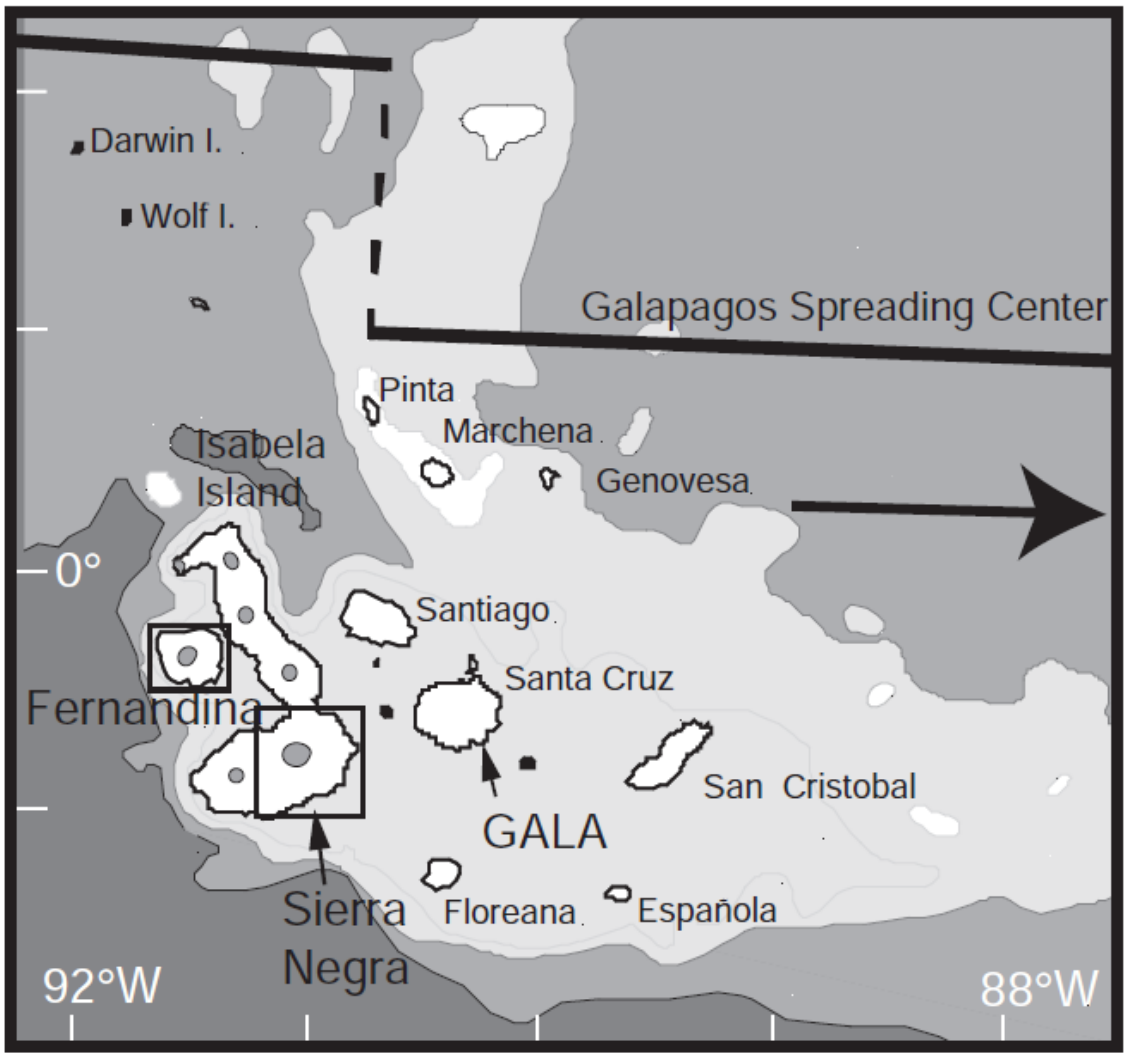

Figure 2.2: Map of Galápagos Islands with Galápagos Spreading Center (GSC) delineated north of the archipelago. Arrows indicate the direction of plate motion. Image is from *Geist et al.* [2006].

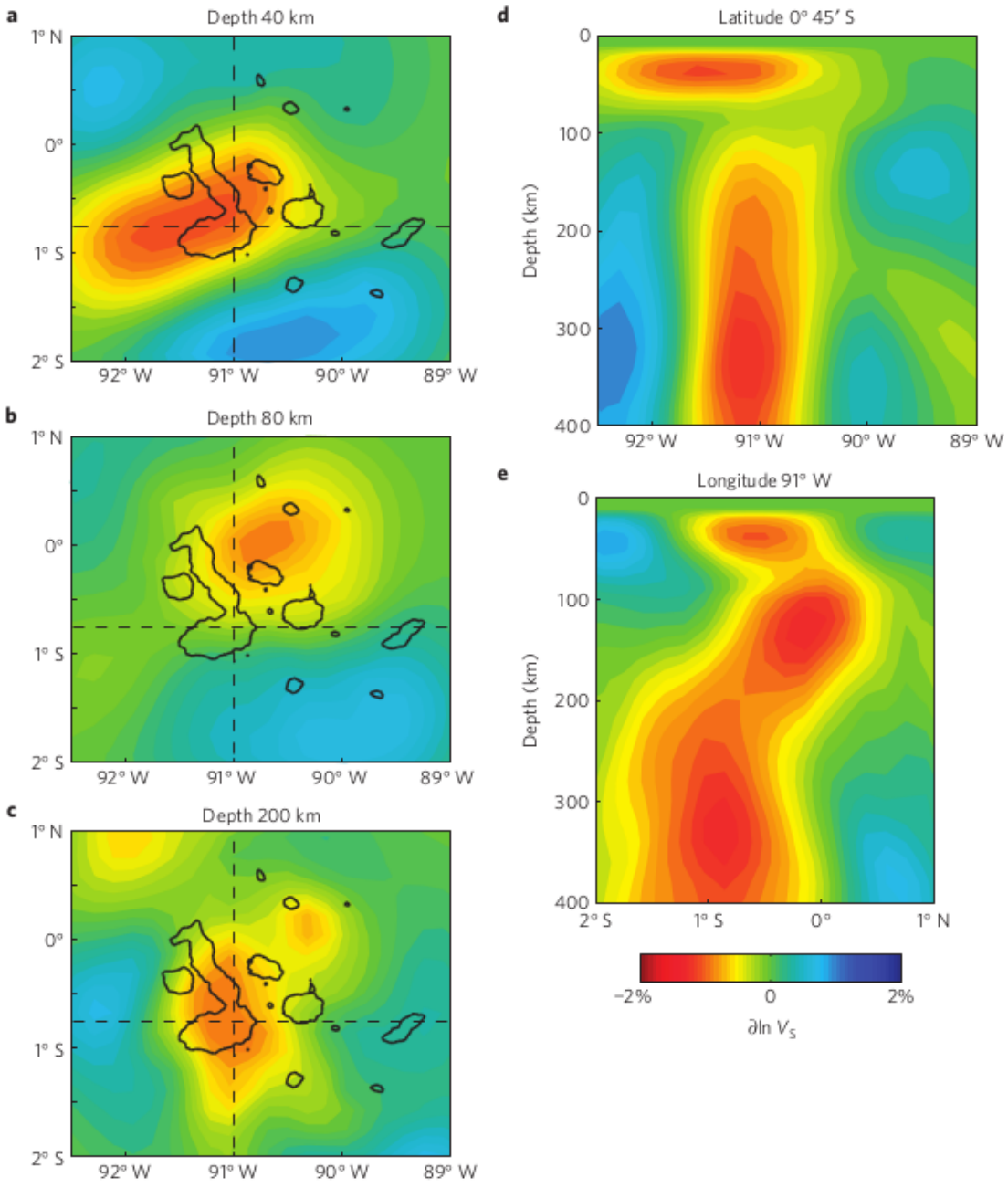

Figure 2.3: Results of tomographic inversion for S-wave velocity structure derived from teleseism events. Color scale denotes the percent deviation from the starting model. (a-c) Map-view of horizontal section at (a) 40 km (b) 80 km and (c) 200 km depth. (d) East-west cross-section at 0°45′ S. (e) North-south cross-section at 91° W. Dashed lines in (a-c) indicate locations of cross sections (d-e). Image and caption are from *Villagomez et al.* [2014].

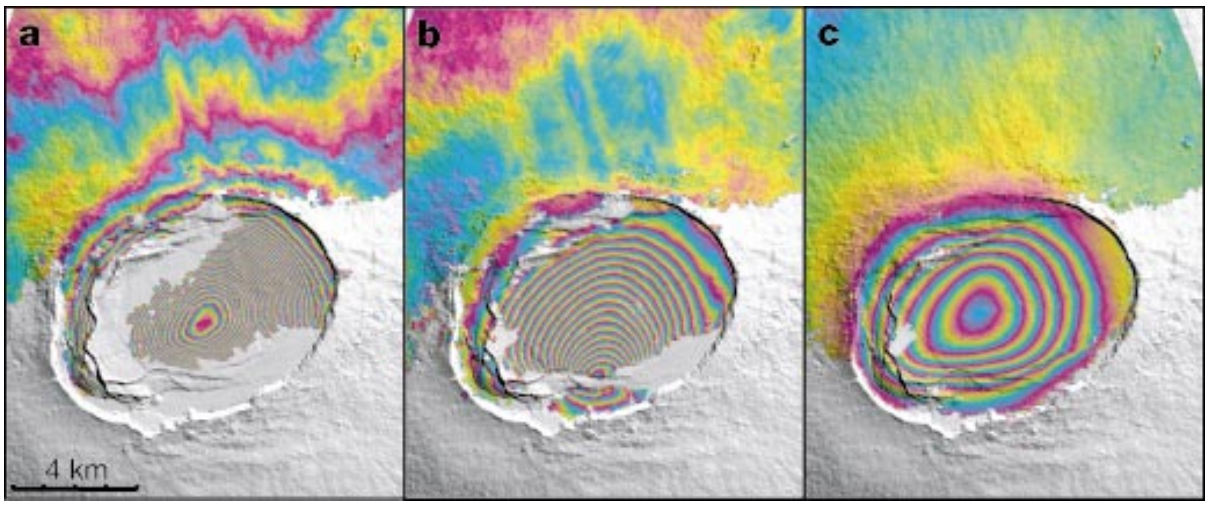

Figure 2.4: Radar interferograms of Sierra Negra volcano showing uplift during three time periods (a) 1992-1997 (5.3 years, descending orbit) (b) 1997-1998 (1.1 years, descending orbit) (c) 1998-1999 (0.5 years, ascending orbit). Each color cycles represents 5 cm LOS displacement. The deformation pattern during the first and third time period is similar, but is markedly different during the intervening period. In (b) the interferometric phase is continuous across the the pre-existing fault in the southern part of the caldera, the location of the proposed trapdoor faulting. This image and caption are from *Amelung et al.* [2000].

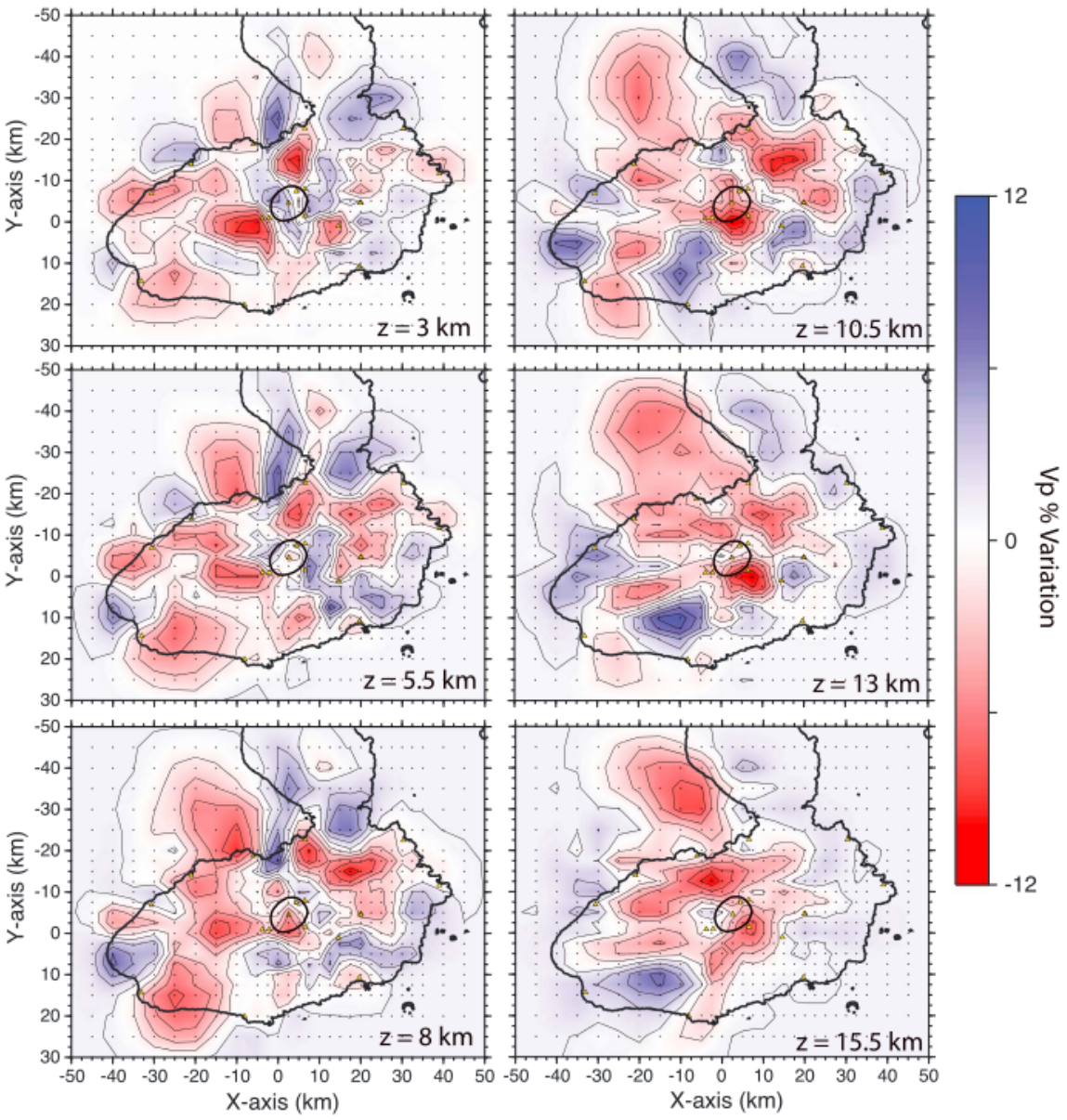

Figure 2.5: P-wave velocity model of the Sierra Negra region of Isabela Island in the Galápagos at depths with the best resolution. Color scale shows the percent variation of V_p with respect to Table 4.2 at each respective depth. Contour lines are in steps of 2%. The thick black line outlines southern Isabela Island and the caldera of Sierra Negra. Crosses indicate coarse grid points. Image and caption are from *Tepp et al.* [2014].

CHAPTER 3.

Seismic Attenuation

Seismic attenuation is the reduction of amplitude of a propagating seismic wave. Amplitude reduction can occur due to redistribution or loss of energy. Geometrical spreading and scattering lead to redistribution of energy. In these processes, the integrated energy of the total wave field remains constant. Geometrical spreading is the exponential decay of amplitude with radius, r. Scattering attenuation is energy partitioning caused by seismic waves propagating through heterogeneous medium.

Anelastic or intrinsic attenuation is the loss of energy of a seismic wave due to internal friction. There are several physical mechanisms that have been proposed to explain intrinsic attenuation including grain or crack boundary sliding and fluid-filled cracks. Frictional sliding along grains and/or cracks predicts that attenuation is frequency-independent across the seismic frequency band [*Walsh*, 1966; *Sato and Fehler*, 2009]. Experimental studies on fluid-filled cracks and pores effect on attenuation have varying results [*Sato and Fehler*, 2009]. It is clear that fluid-motion within pores is one the primary causes of absorption [*Eberhart-Phillips et al.*, 2005; *Winkler and Murphy*, 1995]. However, absorption will vary by pressure, temperature, fluid content, grain-size, fracture-size, etc. [*Kampfmann and Berckhemer*, 1985; *Jackson*, 1993; *Jackson et al.*, 2004; *Faul and Jackson*, 2005; *Jackson and Faul*, 2010]. Characterizing the effects of these rock properties on attenuation is an ongoing problem in experimental rock physics.

Attenuation is described by the inverse of the quality factor, Q, which is the fractional energy loss per cycle. Total attenuation can be described as a summation of scattering and intrinsic attenuation, $Q^{-1} = Q_s^{-1} + Q_i^{-1}$. Laboratory experiments suggest that contributions of each are roughly equal [*Eberhart-Phillips et al.*, 2005]. However, previous

volcano attenuation studies show that scattering dominates at frequencies greater than 10 Hz [*Del Pezzo et al.*, 2006; *De Siena et al.*, 2009].

Using Q, the amplitude of a seismic wave is given by,

$$A(x) = A_0 e^{\frac{-\omega x}{2cQ}} \tag{3.1}$$

where x is the distance traveled, c is the seismic velocity, and ω is the frequency. To simplify this equation, the attenuation operator, t^*, is often used instead of Q, where t^* is related to Q by,

$$t^* = \int_{raypath} \frac{dt}{Q(r)} \tag{3.2}$$

Given Equation 3.2, Equation 3.1 is updated to

$$A(x) = A_0 e^{\frac{-\omega t^*}{2}} \tag{3.3}$$

This equation implies that higher frequencies are more attenuated. This is true for scattering and intrinsic attenuation [*Sato and Fehler*, 2009]. When a pulse travels through an attenuating body, it will gradually lose the higher frequencies. Therefore, higher frequencies in the amplitude spectrum will be reduced. If we assume the phase spectrum is unchanged, then t^* will be a symmetric pulse for a δ-function source [*Shearer*, 2009]. However, the front edge of the pulse will arrive before the theoretical arrival time [*Shearer*, 2009; *Aki and Richards*, 2002]. As a result of this complication, existence of attenuation requires that velocity be frequency-dependent even if Q is frequency-independent [*Liu et al.*, 1976; *Aki and Richards*, 2002].

Q is often approximated as being constant over a given frequency band, usually estimated between $0.001 - 0.1$ Hz. This assumption fails at low and and high frequencies. These end-member values depend on the model or scale of observation. For an absorption band model, the upper frequency fall off is between 0.5-2 Hz [*Warren and Shearer*, 2000].

Mineral physics experiments suggest that Q is related to frequency by $Q^{-1} \sim \omega^{\gamma}$ where $\gamma \approx -0.2$ to -0.3 [*Berckhemer et al.*, 1982; *Jackson et al.*, 2002]. Attenuation tomography studies have conflicting results on the frequency-dependency of Q. *Bellis and Holtzman* [2014] suggests the frequency-dependency of Q could affect measurements of Q^{-1}. This problem should be considered when approaching attenuation tomography studies.

3.1 Measuring Attenuation

There are several methods for measuring attenuation for tomography studies. The following methods will be discussed briefly:

1. t^* Spectral Decay
2. Coda-Normalization
3. Coda Lapse-Time
4. Coda Wave Envelope

This is not an exhaustive list of attenuation tomographic methods.

3.1.1 t^* Spectral Decay

t^* spectral decay is the most common method for measuring total Q^{-1}. As described above, when a seismic wave travels through an attenuating region, high-frequencies are lost. The amplitude spectra contains this high-frequency fall-off and is used to determine t^*. The spectrum also contains high-frequency fall-off of the source and this must be considered in spectral modeling. Another concern with this method is when medium heterogeneity is too high, coherent direct-wave information is disrupted and t^* attenuation calculations are largely affected [*De Siena et al.*, 2013]. Further details on this method are provided in Chapter 4.

3.1.2 Coda-Normalization

Coda-normalization (CN) method is used to determine average Q^{-1} using direct and coda energies [*Aki*, 1980; *Yoshimoto et al.*, 1993; *Del Pezzo et al.*, 2006; *De Siena et al.*, 2009, 2014a]. Path attenuation is calculated by measuring the direct phase-arrival energy and the coda energy for a given lapse time, t_c. When energy is converted to amplitude, the following relationship is obtained [*Aki*, 1980; *Del Pezzo et al.*, 2006],

$$\ln(\frac{A_{ij}^s(f)}{A_{ij}^c(f,t_c)}) \cdot r_{ij} = K(f,t_c) - \pi f r \int_{r_{ij}} \frac{dl}{v(l)Q(l)} \tag{3.4}$$

where A_{ij}^s and $A_{ij}^c(f,t_c)$ are the spectral amplitudes of the S and coda waves, respectively, $K(f,t_c)$ is constant dependent on the average medium properties, $v(l)$ is the velocity along the ray path, and r_{ij} is the ray length. This method assumes homogeneity of the scattering regime at a given frequency and lapse time. *De Siena et al.* [2014a] has developed a MatLAB program of a multi-resolution CN method for application to high-scatter regimes, such as volcanic settings.

3.1.3 Lapse-Time

A major problem with spectral decay method is the convolution of source and attenuation in the amplitude spectra. Coda wave envelopes are independent of source location and orientation at certain epicentral distances and can provide a simple and useful method to measure attenuation [*Aki and Chouet*, 1975]. In a single scattering model, the coda decay is modeled as,

$$E(t_c,f) = S(f)t_c^{-2}e^{\frac{-2\pi f t}{Q_c}} \tag{3.5}$$

where E is the power spectrum, $S(f)$ is a frequency-dependent source or site term, t_c is the lapse time, and f is the frequency. In a single-scatter model, Q_c depends on scattering and absorption [*Shapiro et al.*, 2000]. More recently, generation of coda

waves in a multiple-scattering regime was confirmed. This implies at long lapse time, coda waves follow a diffusive regime [*Shapiro et al.*, 2000]. *Calvet and Margerin* [2013] suggests that given a certain lapse time and window length, Q_i^{-1} can be approximated from Q_c^{-1}. Therefore, this method offers a way to quantify the contribution of absorption to the total attenuation.

3.1.4 Coda Wave Envelope

Coda waves are interpreted as the arrival of scattered waves due to heterogeneities between source and receiver [*Aki*, 1969]. Therefore, variation in the coda power envelope can be used to estimate spatial variation in scattering [*Nishigami*, 1991]. The coda energy density , $E(\mathbf{x}, t)$ for a receiver at position $\mathbf{x}$ and lapse time t can be modeled by assuming single isotropic scattering in a medium filled by $Nscat$ number of randomly and uniformly distributed scatters at position, $\mathbf{z}$ [*Tramelli et al.*, 2006].

$$E_u(\mathbf{x}, t) = \frac{W g_0}{V_0 (4\pi)^2} e^{-2\pi f t Q_C^{-1}} \times \sum_{i=1}^{Nscat} \delta(t - \frac{r_a(\mathbf{z}_i) + r_b(\mathbf{z}_i)}{V_0}) \frac{1}{r_a^2(\mathbf{z}_i) r_b^2(\mathbf{z}_i)} \tag{3.6}$$

where g_0 is the scattering coefficient, r_a is the source-to-scatter distance, r_b is the scatter-to-receiver distance, δ is the Dirac delta function, W is the total energy at the source, f is the frequency, and Q_C^{-1} is the total inverse Q-coda. When distribution of scatterers is hetergeneous, g_0 is dependent on $\mathbf{z}$. Equation 3.6 is modified to,

$$E_{nu}(\mathbf{x}, t) = \frac{W g_0}{V_0 (4\pi)^2} e^{-2\pi f t Q_C^{-1}} x \sum_{i=1}^{Nscat} \delta(t - \frac{r_a(\mathbf{z}_i) + r_b(\mathbf{z}_i)}{V_0}) \frac{\alpha_i}{r_a^2(\mathbf{z}_i) r_b^2(\mathbf{z}_i)} \tag{3.7}$$

where $g_0 \alpha_i = g(\mathbf{z}_i)$.

For small distances from the earthquake hypocenter, Equation 3.7 is approximated as,

$$E_u(t) \simeq \frac{W g_0}{t^2} e^{-2\pi f t Q_C^{-1}} \tag{3.8}$$

Using this approximation, estimates of g_0 and Q_C^{-1} can be determined. α_i can be calculated by solving the linear system:

$$\frac{\epsilon_{nu}(\mathbf{x}_m)_{jk}}{\epsilon_u(\mathbf{x}_m)_{jk}} = \frac{\sum_{i=1}^{Nscat}(\alpha_i / r_{amk}^2(\mathbf{z}_i) r_{bmk}^2(\mathbf{z}_i))}{\sum_{i=1}^{Nscat}(1 / r_{amk}^2(\mathbf{z}_i) r_{bmk}^2(\mathbf{z}_i))} \tag{3.9}$$

where $\epsilon_{nu}(\mathbf{x}_m)_{jk}$ and $\epsilon_u(\mathbf{x}_m)_{jk}$ are the integrated energy density from Equations 3.6 and 3.7, respectively. The scattering coefficient, $g(\mathbf{z}_i)$, is solved by multiplying g_0 and α_i. Refer to *Nishigami* [1991] and *Tramelli et al.* [2006] for complete discussion of this method.

3.2 Volcano Attenuation Studies

Attenuation is an important tool for studying volcanic systems. Although velocity studies are more common and better understood, attenuation is more sensitive to rock properties, in particular temperature gradients and fluid permeation. The methods described above and others have been used to image the attenuation structure of volcanoes. Modeling is often difficult due to data noise and high scatter, particularly in volcanic cones where signal coherence is quickly lost over a short time period. It is best to model attenuation using multiple methods to qualify the accuracy of the result. t^* spectral decay and coda-normalization methods both determine total Q^{-1}. Therefore, results should be similar across the methods. Furthermore, lapse time and coda envelope methods could be used to quantify the contribution of scattering and absorption to the total attenuation. Multiple-method studies can distinguish differences in the causes of high attenuation signal (i.e. scattering heterogeneities vs. fluid-filled pores). Multiple-method volcanic studies have successfully imaged zones of magma accumulation, fluid permeation, and magma ascent [*Del Pezzo et al.*, 2006; *De Siena et al.*, 2009, 2010, 2014b; *Ohlendorf et al.*, 2014].

CHAPTER 4.

Attenuation Tomography of Sierra Negra

4.1 Introduction

In this study, attenuation tomography was used to create the first fine-scale seismic image of the shallow magma reservoir beneath Sierra Negra. Although geodetic studies indicated the presence of a shallow magma reservoir at 2.1 km [*Amelung et al.*, 2000; *Jonsson et al.*, 2005; *Yun et al.*, 2006; *Chadwick et al.*, 2006; *Geist et al.*, 2008], this structure was not imaged seismically prior to this study.

Seismic attenuation is strongly dependent on temperature and fluid content [*Kampfmann and Berckhemer*, 1985; *Jackson*, 1993] and is particularly useful in studying volcanic media where high attenuation is interpreted as magma accumulation [*Lees*, 2007]. The spectral decay method is used following a similar approach as *Lees and Lindley* [1994] to image the attenuation structure beneath Sierra Negra. Despite difficulties in modeling and high scatter, this method has successfully imaged attenuation structures in various volcanic media (e.g. hotspot, composite volcano) [*De Siena et al.*, 2009, 2010; *Koulakov et al.*, 2014; *Ohlendorf et al.*, 2014; *Lin et al.*, 2015]. We interpret our Q_p^{-1} model in context of current V_p [*Tepp et al.*, 2014], initial group velocity, U_g, derived from ambient noise tomography [*Seats et al., in prep*, 2016], and geodetic models.

4.2 Data

We analyzed data from the SIGNET seismic array deployed on Isabela Island from July 2009 to June 2011 in collaboration between Instituto Geofisico Nacional Escuela Politecnica, University of Rochester, University of Miami, University of Idaho, and the Charles Darwin Foundation. Figure 4.1 shows the 15 temporary broadband stations. During service runs in 2010, stations GS08, GS14, and GS16 settings and/or locations

were changed and were renamed to GS8A, GS18, and GS17 to reflect these changes. Sampling frequency was 40 Hz and 50 Hz for Guralp 3T and Nanometrics Trillium 120P sensors, respectively. Refer to Table 4.1 for further station and equipment detail.

P- and S- wave phase arrivals and error bars were manually picked using the RCran package, RSEIS [*Lees*, 2015a]. Earthquakes were located with Rquake package [*Lees*, 2015b] using the P- and S- wave arrivals and the 1D velocity model from *Tepp et al.* [2014] shown in Table 4.2 and Figure 4.2. Figure 4.3 shows the 309 (large circles) of the 1727 recorded events that were used in the final inversion. Poorly located events and events located outside the 30 x 30 km grid (black dashed line in Figure 4.3) were excluded. Initially, a larger grid similar to *Tepp et al.* [2014] was used. This resulted in clustering bias, smearing, and poor resolution beneath the caldera at shallow depths.

Table 4.1: SIGNET array station information

Station	Dates Active	Latitude	Longitude	Instrument	Hz)
GS01	2009/07/23-2011/06/13	-0.646600	-90.877700	CMG3T	50
GS02	2009/07/23-2011/06/14	-0.743400	-90.799700	CMG3T	50
GS03	2009/07/23-2011/01/15	-1.031200	-91.223000	CMG3T	50
GS04	2009/07/25-2010/06/21	-0.645800	-91.093000	CMG3T	50
GS05	2009/07/25-2011/06/15	-0.722400	-91.338100	CMG3T	50
GS06	2009/07/26-2011/06/15	-0.680400	-91.203900	CMG3T	50
GS07	2009/07/26-2011/06/16	-0.787700	-91.424700	CMG3T	50
GS08	2009/07/27-2010/06/21	-0.979200	-91.446800	Tril Comp	50
GS8A	2010/06/21-2011/06/17	-0.979200	-91.446800	Tril Comp	50
GS09	2009/07/24-2011/06/12	-0.782900	-91.110300	CMG3T	50
GS10	2009/07/23-2011/06/13	-0.837100	-91.091500	CMG3T	50
GS11	2009/07/26-2011/06/14	-0.947400	-90.974400	CMG3T	50
GS12	2009/07/26-2011/06/15	-0.859800	-91.019200	CMG3T	50
GS13	2009/07/23-2011/06/12	-0.777800	-91.092100	CMG3T	50
GS14	2009/07/29-2010/06/21	-0.808300	-90.970300	Tril120PA	40
GS15	2009/07/30-2011/06/19	-0.809500	-91.127300	Tril120PA	40
GS16	2009/07/31-2010/06/21	-0.842000	-91.184300	Tril120PA	40
GS17	2010/11/04-2011/06/15	-0.841100	-91.169600	Tril120PA	40
GS18	2010/11/07-2011/06/15	-0.809000	-90.971200	Tril120PA	40

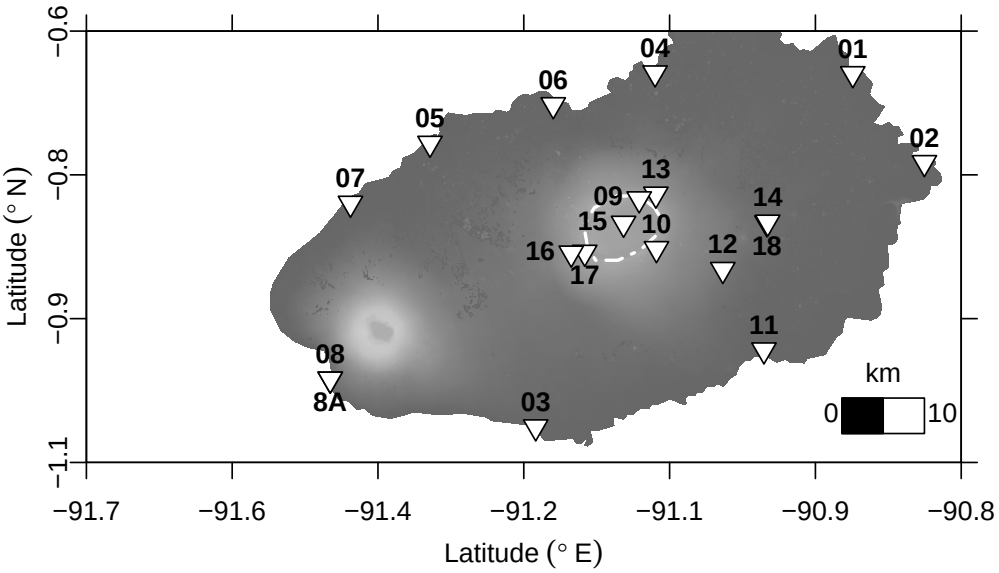

Figure 4.1: Map of southern Isabela Island and Sierra Negra Volcano (white-dashed ellipse) with SIGNET array stations shown in light-gray triangles.

Layer	Depth	V_p (km/s))	V_s (km/s)
1	0	4.290	2.480
2	0.5	4.370	2.528
3	3	5.240	3.025
4	5.5	6.083	3.515
5	8	6.470	3.740
6	10.5	6.700	3.865
7	13.0	6.89	3.978

Table 4.2: 1-D velocity model used for earthquake location and background model for body-wave tomography.

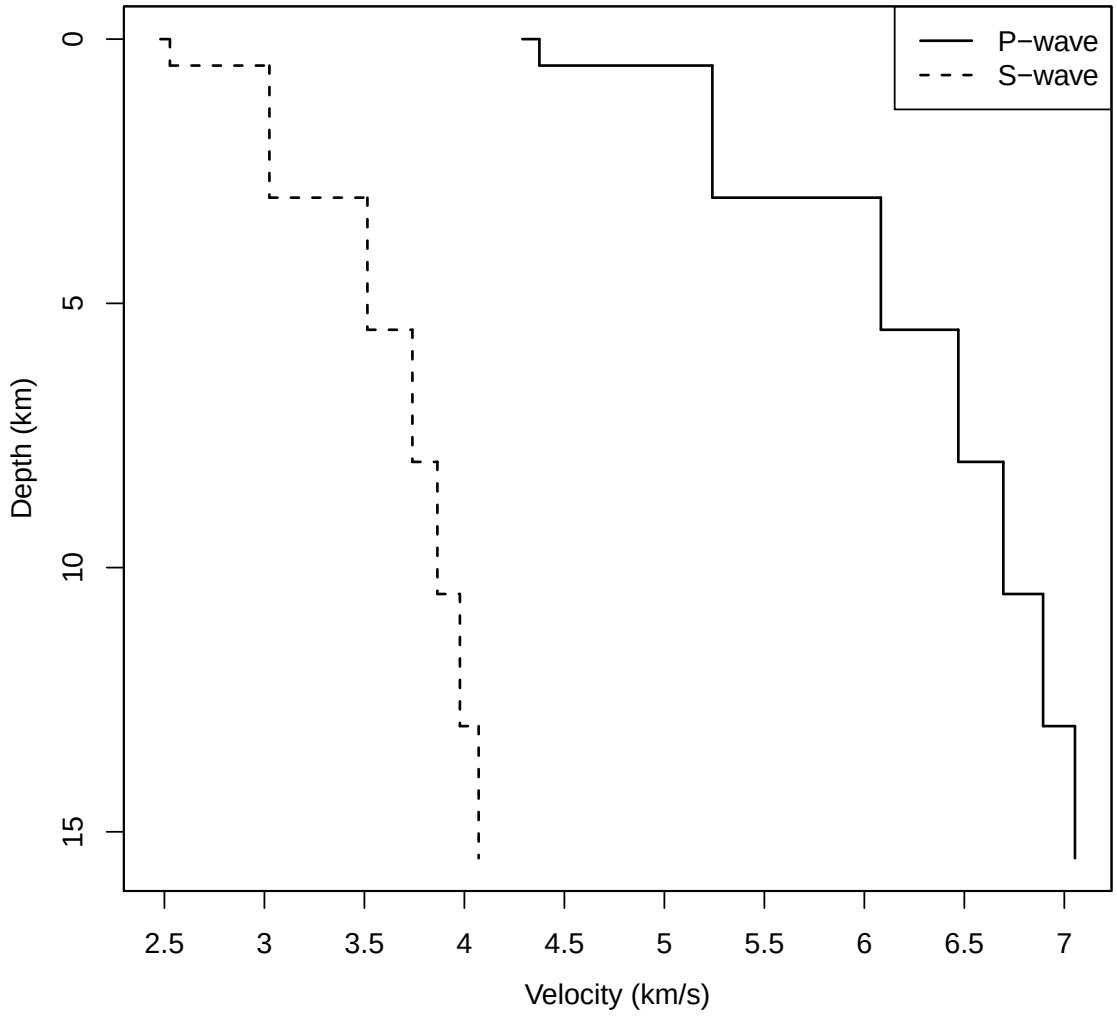

Figure 4.2: 1-D velocity model used for initial earthquake locations and background model for body-wave tomography by *Tepp et al.* [2014].

4.3 Methodology

4.3.1 Spectral Decay Method

The 3-D attenuation subsurface structure was determined using the spectral decay method in which t^*, the attenuation operator, was estimated for each ray path by modeling the amplitude spectrum of earthquake ground displacement. The observed spectrum, A_{ij}, of event i at station j is modeled as [*Scherbaum*, 1990]

$$A_{ij}(f) = S_i(f) \cdot I_j(f) \cdot R_j(f) \cdot B_{ij}(f) \tag{4.1}$$

where f is the frequency, $S(f)$ is the far-field source spectrum, $I(f)$ is the instrument response, $R(f)$ is the site response, and $B(f)$ is the absorption spectrum.

$S(f)$ is modeled as

$$S(f) = \frac{\Omega_0}{\left(1 + \left(\frac{f}{f_c}\right)^{n\gamma}\right)^{1/n}} \tag{4.2}$$

where f_c is the source corner frequency, Ω_0 is the low-frequency plateau amplitude, and γ is the fall-off of the displacement specra above f_c.

The absorption along the ray path is described by

$$B(f) = e^{-\pi f^{1-\alpha} t_0^*} \tag{4.3}$$

where t_0^* is the attenuation parameter and α is the frequency dependence of attenuation.

Instrument response was removed prior to computing the amplitude displacement spectra. Thus $I(f)$ is not included in the spectral inversion. Unusual variation observed in spectra for a single station and/or nearby stations would suggest a local site response. Often this variation is observed as a bump in the amplitude spectra [*Bennington et al.*, 2008]. This behavior was not observed in the data and near-surface geology is not ex-

pected to vary significantly by station. Therefore, $R(f)$ are not included in the spectral inversion.

Substituting Equations 4.2 and 4.3 into Equation 4.1 produces,

$$A(f) = \frac{\Omega_0 e^{-\pi f t^*}}{\left(1 + \left(\frac{f}{f_c}\right)^{n\gamma}\right)^{1/n}} \tag{4.4}$$

$$t^* = t_0^* f^{-\alpha} \tag{4.5}$$

When $n = 1$, the model is equivalent to the f^2 Brune source model [*Brune*, 1970]. This model is assumed for several earthquake source studies [e.g *Randall*, 1973] and spectral decay attenuation tomography [e.g. *Scherbaum*, 1990; *Rietbrock*, 2001; *Eberhart-Phillips and Chadwick*, 2002]. We assumed a modification of the f^2 model with $n = 2$ [*Boatwright*, 1978; *Abercrombie*, 1995; *Lindley and Archuleta*, 1992; *Lees and Lindley*, 1994] which produces a sharper corner and better fit to the spectra.

4.3.2 Computation of Amplitude Spectra

The amplitude spectra were calculated for all P-wave arrivals using the multi-taper method of the fast Fourier transform (FFT) [*Lees and Park*, 1995]. The resolution of the spectra is dependent on the sampling frequency and time window selection. Seismograms with P-S time differences less than the selected time window were excluded. The data set is dominated by shallow caldera events leading to small P-S times. Given the small P-S times, a sampling rate of $40 - 50$ Hz is less than ideal for FFT.

Amplitude spectra were computed several times for 1, 2, 3, and 4 s time windows to determine the best trade-off between spectral resolution and usable data. Increasing the time window increased mean residual RMS (Figure 4.4). This was expected since improved resolution allows for greater variability in the amplitude spectra. Figure 4.5 displays the variation in mean t^* for several stations at varying time windows. There is

no significant variation in t^* suggesting that the window lengths resolve the same model. The amplitude spectra were visually inspected as confirmation. Therefore, a 1 s time-window was used to optimize the number of t^* values. A noise spectrum was calculated from a 1 s time window selected prior to the arrival. In order to ensure quality t^* values, only spectra with SNR > 2.5 across a continuous frequency band from 2 to 15 Hz were allowed.

4.3.3 Spectral Modeling

The amplitude source spectra were modeled using Equation 4.4. It is not possible to obtain a unique best fit solution with the five free parameters: γ, α, t^*, f_c, and Ω_0. Therefore, γ and α were fixed, while initially f_c, t^*, and Ω_0 were allowed to vary. γ is set to a sequence of values between 0 and 3 with $\alpha = 0$ for determine the optimum γ. Figure 4.6 corroborates previous findings that $\gamma = 2$ provides the best fit results [*Boatwright*, 1978; *Scherbaum*, 1990; *Lindley and Archuleta*, 1992; *Lees and Lindley*, 1994; *Abercrombie*, 1995; *Rietbrock*, 2001; *Eberhart-Phillips and Chadwick*, 2002].

Although laboratory studies determined that seismic attenuation is a frequency-dependent process which could affect t^* results [*Bellis and Holtzman*, 2014], tomography studies have conflicting results for α. Previous studies suggested that $-1 < \alpha < 0$ ($0 < \alpha < 1$ if using $Q = Q_0 \cdot f^\alpha$ [*Lindley and Archuleta*, 1992]) provides the best fit to the amplitude spectra [*Hough et al.*, 1999; *Lindley and Archuleta*, 1992; *Sarker and Abers*, 1998]. Other studies found that frequency-independent Q ($\alpha = 0$) produces the best fit or an equivalent fit to frequency-dependent Q, in which case frequency-independent Q is assumed for model simplicity [*Scherbaum*, 1990; *Lees and Lindley*, 1994; *Rietbrock*, 2001; *De Lorenzo et al.*, 2010]. Due to these varying results, spectral modeling was repeated several times with α set to fixed values between -1 and 1. Figure 4.7 shows the residual RMS of modeling for various α. Although attenuation results were similar for all α, resolution and recovery varied significantly due to discrepencies in the amount of usable

t^* values. The mean residual RMS is minimized and number of usable t^* is maximized when $\alpha = -0.2$. Therefore, $\alpha = -0.2$ was used for the final inversion.

The Levenberg-Marquardt method was used to model the spectrum. Initially, t^*, f_c, and Ω_0 were allowed to vary freely, with the exception that extremely low and high outliers of f_c were not allowed. Figure 4.8 displays box plots of the t^* and f_c by station and colored by mean residual RMS of the initial model. Stations are ordered by distance from the caldera. t^* range from near 0 to 0.08. Stations further from the caldera have higher median t^* than nearby stations. Given a caldera event, stations further from the caldera record information that traveled further which should result in greater t^* (i.e. more attenuated). Furthermore, stations near the caldera have high t^* as well, which could suggest high attenuation in this region. For complex and hetergeneous regions such as a volcano, t^* distribution is likely complex.

Initial modeling results in large fluctuations ($2-15$ Hz) in f_c (Figure 4.8b). Assuming similar source mechanisms, f_c should be more constrained than indicated by initial modeling. Figure 4.10 depicts the seismograms, spectra, and unconstrained modeling results for the same event recorded at stations GS12, GS13, and GS14. f_c varies by station in the initial model, despite being a source parameter. This variability is likely due to a trade-off between t^* and f_c which occurs when the two parameters are unconstrained [*Lees and Lindley*, 1994].

Therefore, a second inversion was done, where f_c was constrained to the mean f_c for all ray paths of an event. The mean f_c was iteratively solved by limiting f_c to within the mean $\pm$ one standard deviation of the previous f_c until convergence to a single solution. A summary of the steps used to solve the constrained t^* results is listed below.

1. Determine initial Ω_0, f_c, and t^* by fitting two lines to spectra
2. Use the $\mu \pm \sigma$ of the initial f_c as bounds for search region for f_c
3. Recalculate μ and σ for new f_c

4. Repeat steps 2 and 3 until f_c converges to a single solution for all ray paths for the event

5. Complete for all events

Figure 4.9 displays box plots of the t^* and f_c for the final constrained model. Constrained t^* values are similar to the initial t^* values. Variation in f_c is significantly reduced, but the mean residual RMS increased. Figure 4.11 depicts the seismograms, spectra, and constrained modeling results for the same event and stations as shown in Figure 4.11. When f_c is allowed to vary freely, the model can better fit the data, but variation in f_c is physically infeasible (i.e. f_c differs by ray path from a single source). When f_c is constrained, there is less freedom in modeling, but the results are physically reasonable. The residual RMS histogram for the constrained model is shown in Figure 4.12. The mean residual RMS for all stations is low. A total of 2336 constrained t^* values were obtained. Only 930 of these t^* values correspond to ray paths within the selected grid region with a SNR > 2.5 and were used to determine Q_p^{-1}.

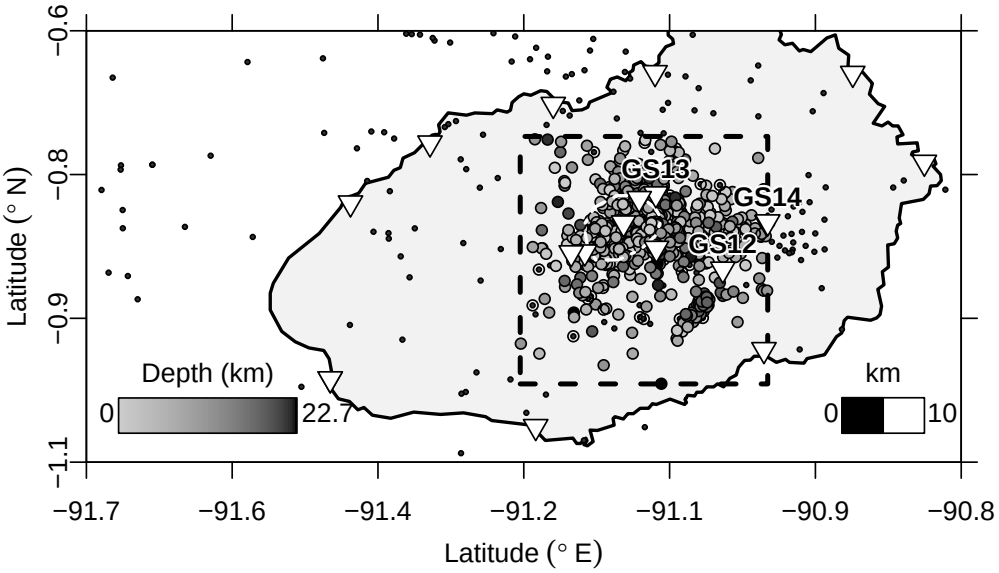

Figure 4.3: Map of southern Isabela Island and Sierra Negra caldera (white-dashed ellipse) with SIGNET array stations shown in light-gray triangles. The black, dashed rectangle outlines the grid boundary and the region in which earthquakes and stations were limited. Earthquakes included in the inversion are shown as large circles colored by depth. Excluded earthquakes are shown as small black circles. Stations GS12, GS13, and GS14 are labeled and correspond to the seismograms and spectra shown in Figures 4.10 and 4.11. The other stations located within the grid boundaries are used in the inversion, but are not labeled.

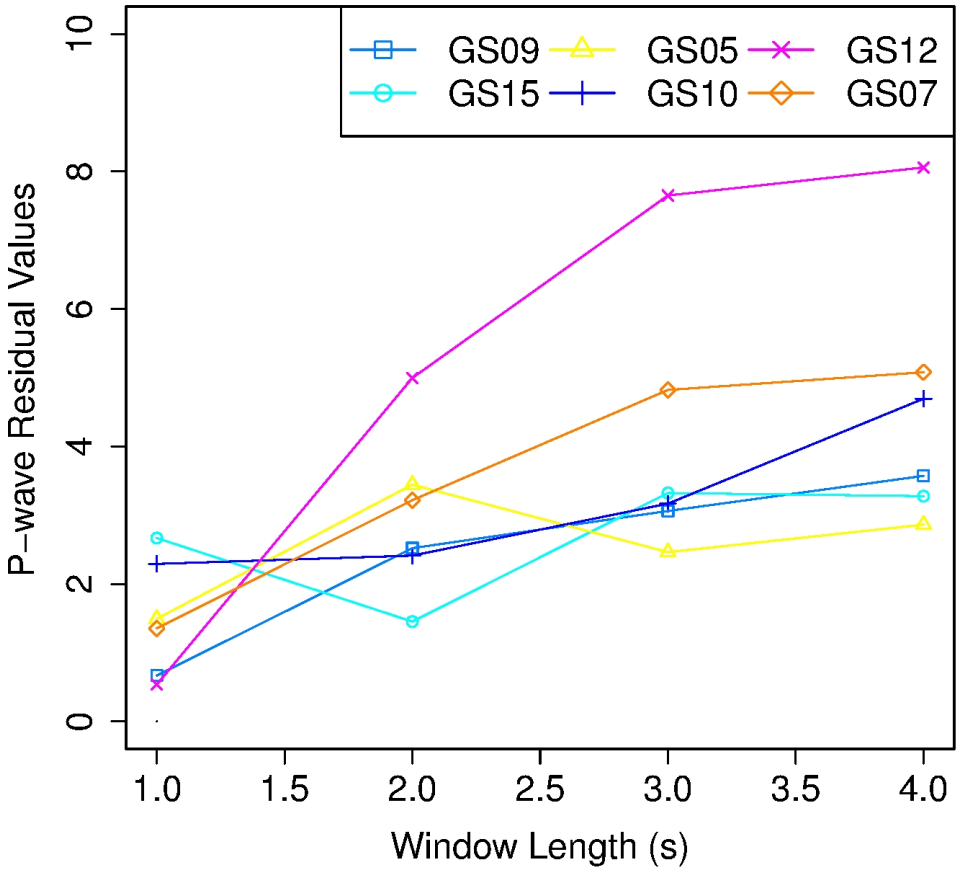

Figure 4.4: Spectral modeling mean residual RMS for various stations as a function of FFT window length.

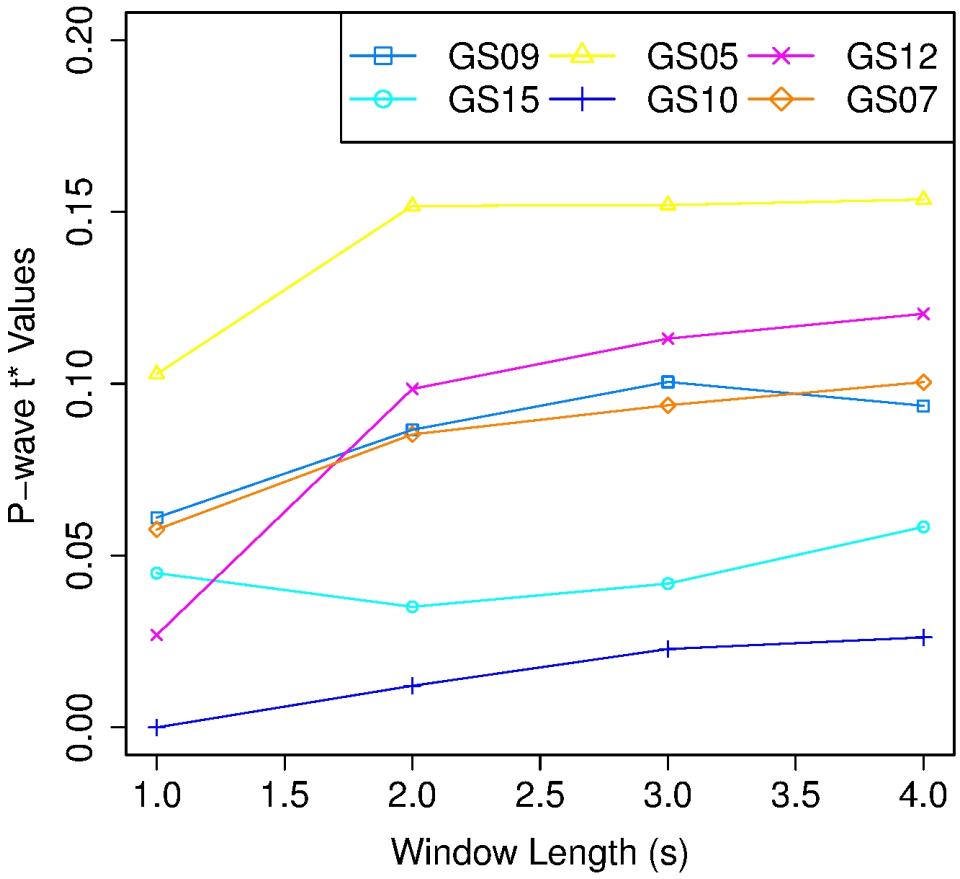

Figure 4.5: Spectral modeling mean t^* for various stations as a function of FFT window length.

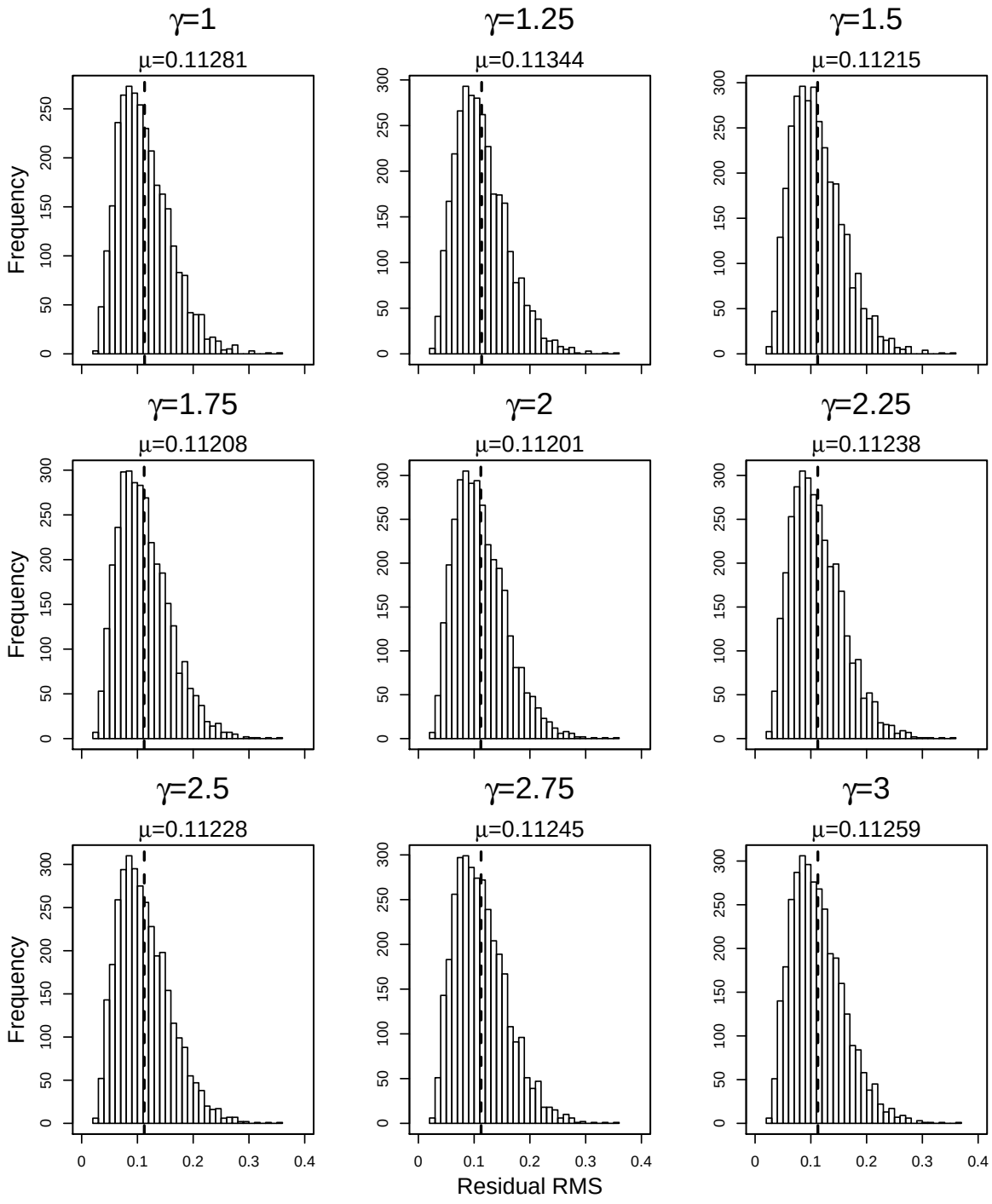

Figure 4.6: Residual root mean squared (RMS) from spectral modeling for various γ. The residual norm is minimized when $\gamma = 2$. This is consistent with previous attenuation tomography studies.

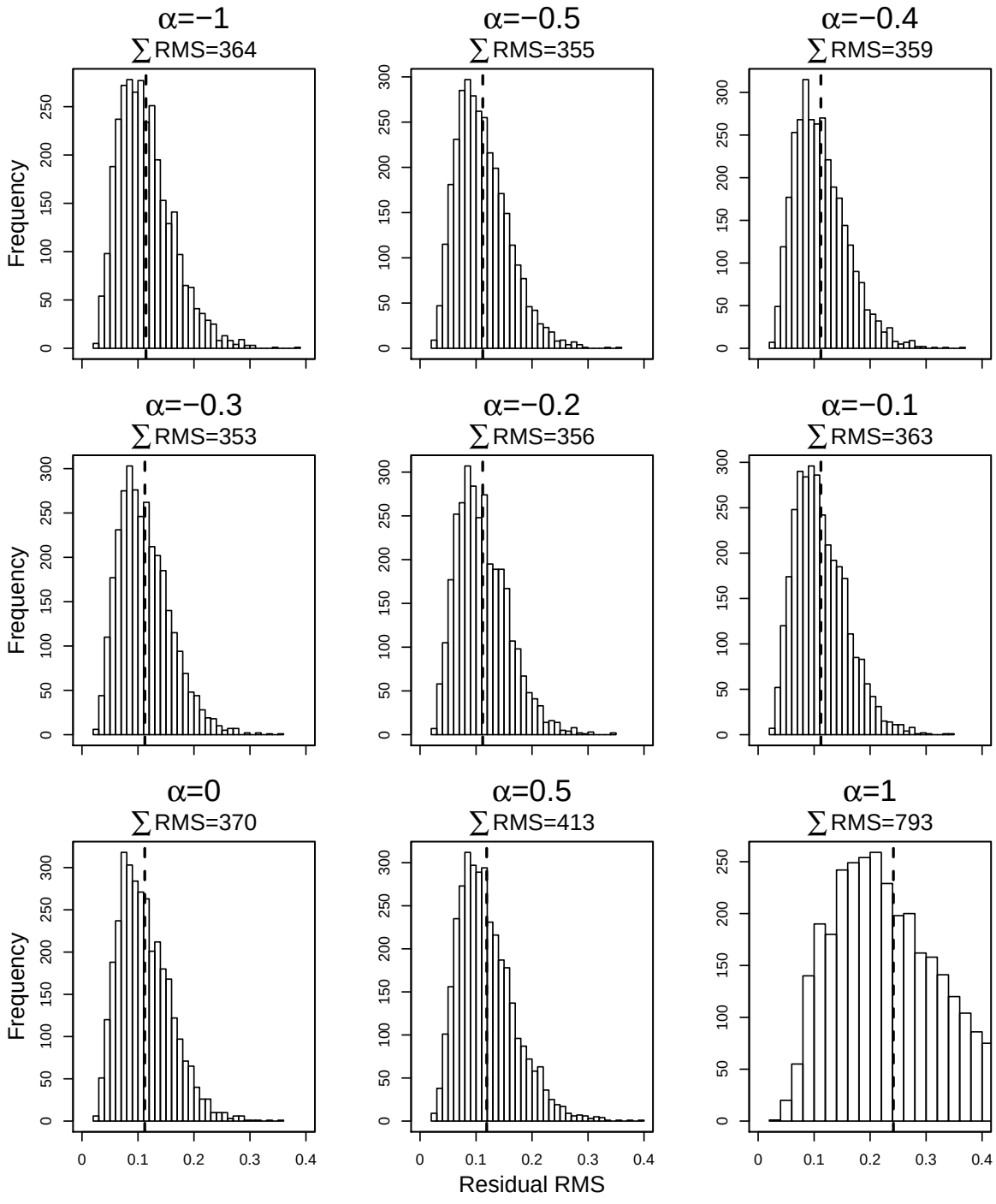

Figure 4.7: Residual root mean squared values from spectral modeling for various α. Although the sum of the residuals is minimized for $\alpha = -0.3$, the mean of the residuals is minimized and number of t^* are maximized when $\alpha = -0.2$. Therefore, $\alpha = -0.2$ was used for the final modeling.

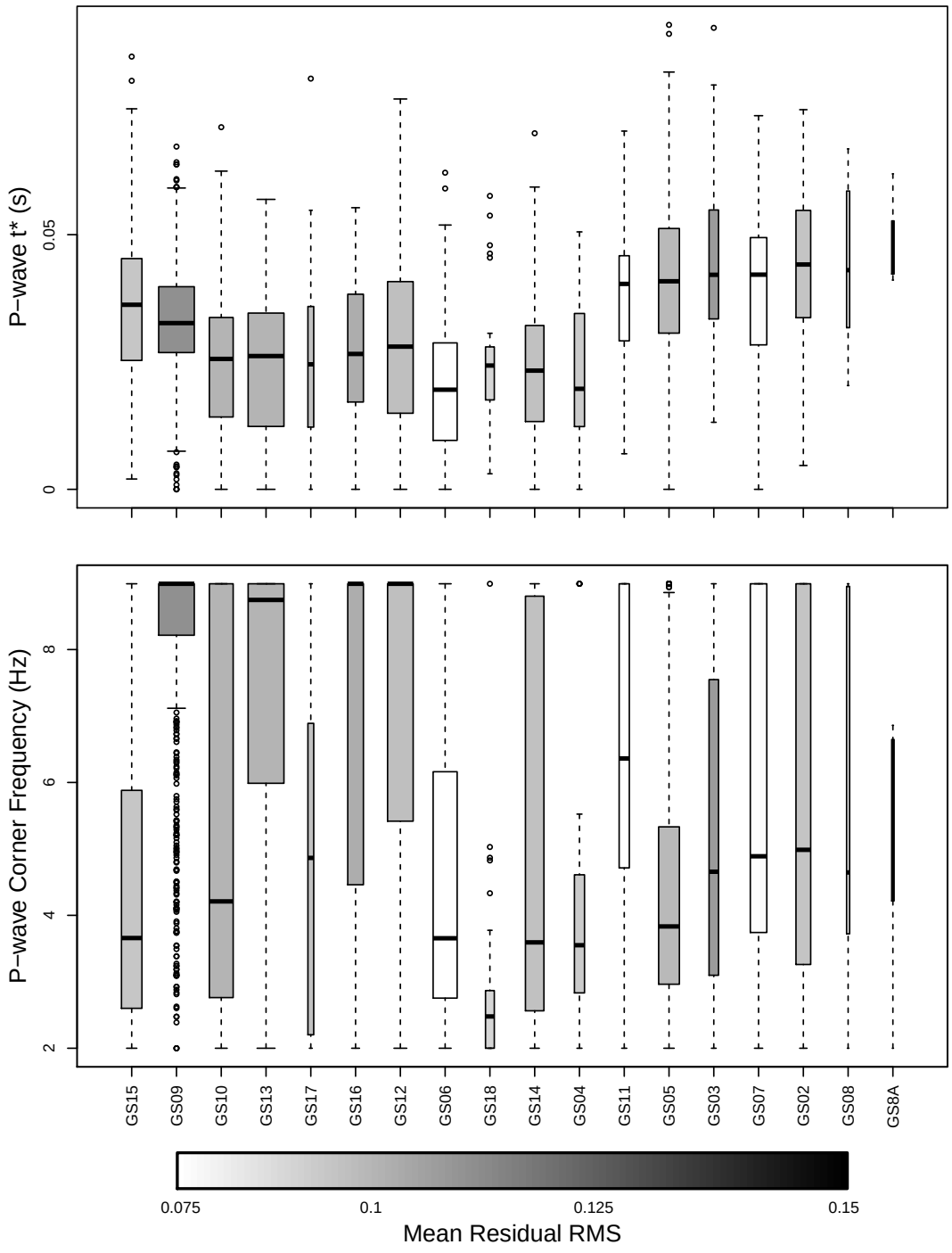

Figure 4.8: Box plot of (a) t^* (b) f_c distribution from unconstrained spectral modeling colored by mean residual RMS.

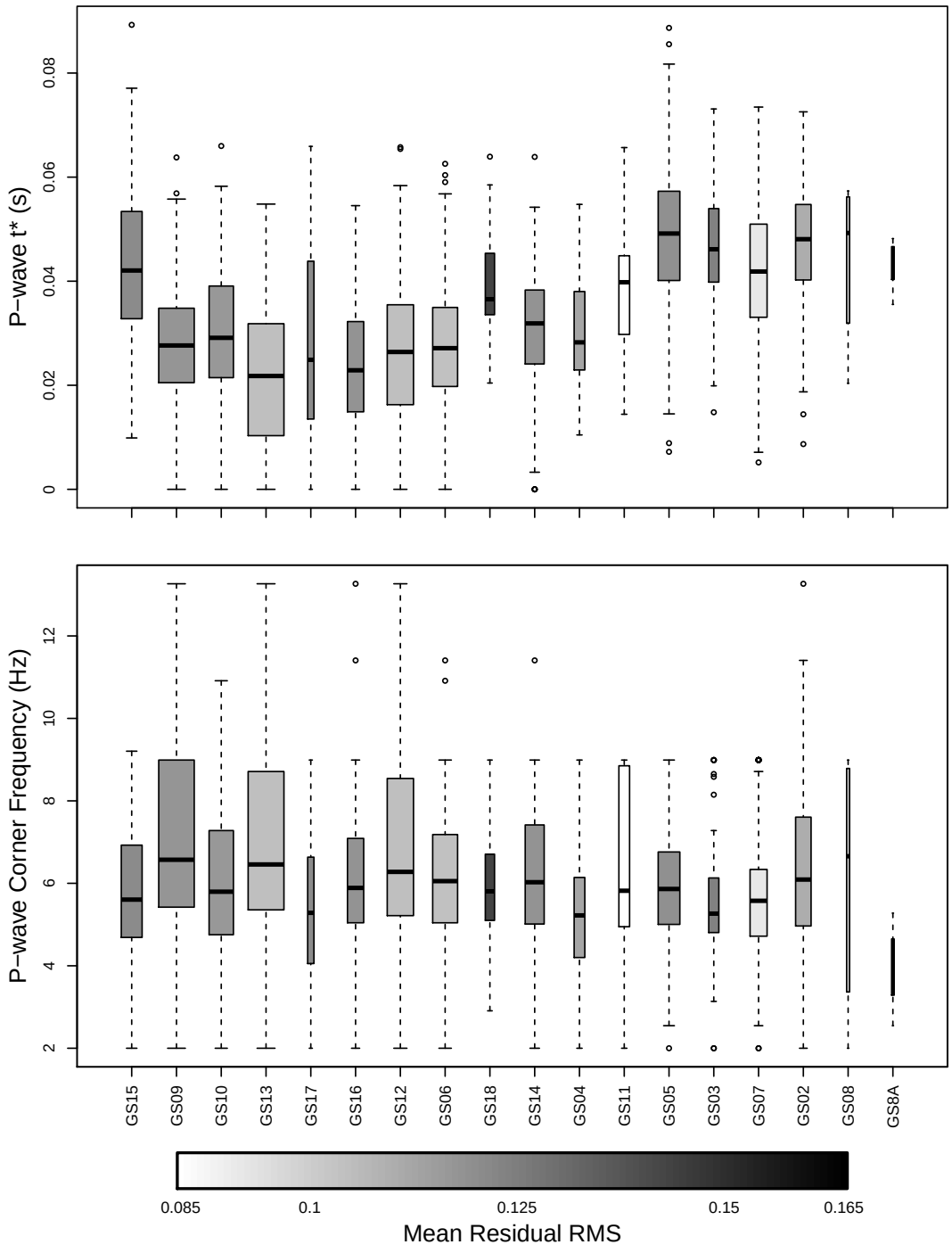

Figure 4.9: Box plot of (a) t^* (b) f_c distribution from constrained spectral modeling colored by mean residual RMS.

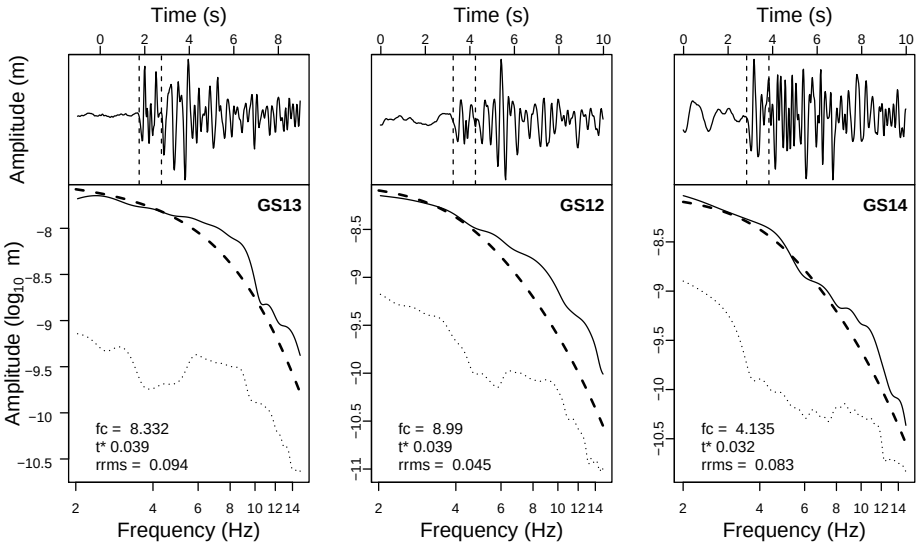

Figure 4.10: Examples of P-wave seismograms and spectra of the same earthquake recorded at stations GS13, GS12, and GS14. The dashed lines on the seismograms indicate the selection window for the computation of the fast Fourier transform. P-wave spectra, unconstrained spectral fits, and noise spectra are shown by solid, dashed, and dotted lines respectively. t^*, f_c, and residual RMS are shown in the bottom right corner of the spectra plot.

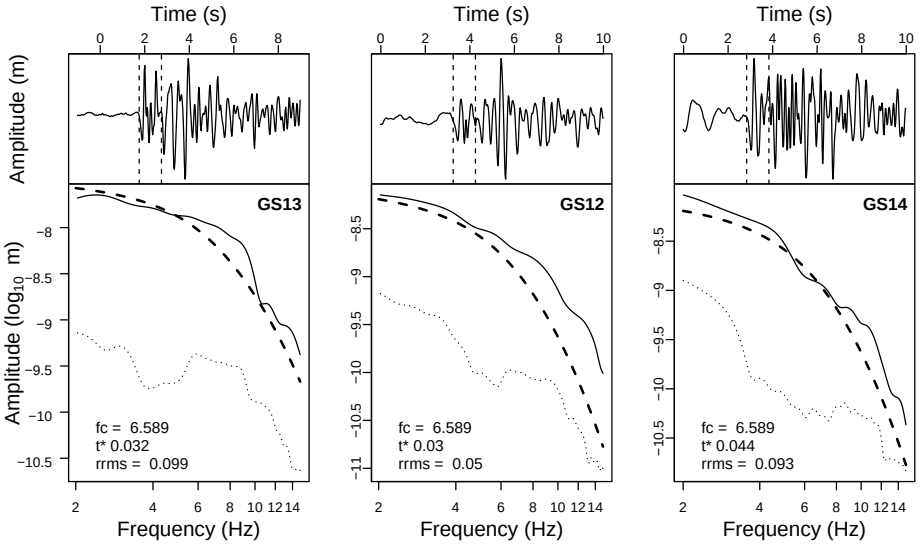

Figure 4.11: Examples of P-wave seismograms and spectra of the same earthquake recorded at stations GS13, GS12, and GS14. The dashed lines on the seismograms indicate the selection window for the computation of the fast Fourier transform. P-wave spectra, constrained spectral fits, and noise spectra are shown by solid, dashed, and dotted lines respectively. t^*, f_c, and residual RMS are shown in the bottom right corner of the spectra plot.

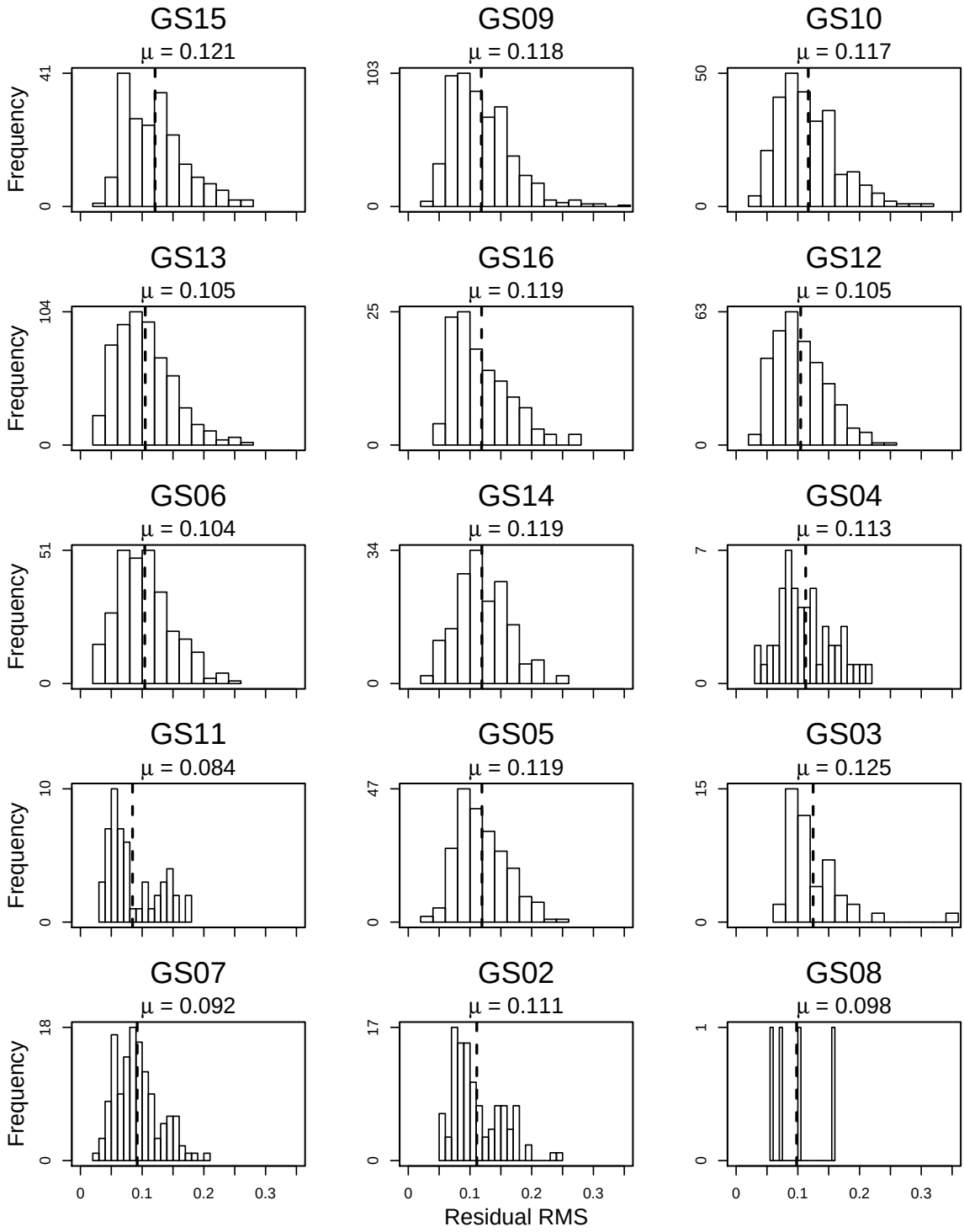

Figure 4.12: Residual root mean squared (RMS) of constrained spectral modeling results by station.

4.3.4 Q_p^{-1} Inversion

The attenuation, Q^{-1}, can be determined from t^* using

$$t^* = \int_{raypath} \frac{1}{Q(x,y,z)} \cdot \frac{1}{v(x,y,z)} \cdot dr(x,y,z) \tag{4.6}$$

where $v(x,y,z)$ is the 3-D velocity model derived from P-wave body-wave tomography [*Tepp et al.*, 2014]. Equation 4.6 was used to obtain a Q_p^{-1} model. The line integral was discretized into 0.5 x 0.5 km blocks at depths of 0, 0.5, 3, 5.5, 8, 10.5, and 13 km, where the attenuation is assumed constant in each block. When discretized, the line integral can be represented by the general inverse problem,

$$\mathbf{Ax} = \mathbf{b} \tag{4.7}$$

where

$$\mathbf{A} = \begin{bmatrix} l_{11}\cdot s_1 & l_{12}\cdot s_2 & l_{13}\cdot s_3 & \dots & l_{1n}\cdot s_n \\ l_{21}\cdot s_1 & l_{22}\cdot s_2 & l_{23}\cdot s_3 & \dots & l_{2n}\cdot s_n \\ \vdots & \vdots & \vdots & \ddots & \vdots \\ l_{d1}\cdot s_1 & l_{d2}\cdot s_2 & l_{d3}\cdot s_3 & \dots & l_{dn}\cdot s_n \end{bmatrix} \mathbf{b} = \begin{bmatrix} \Delta {t^*}_1 \\ \Delta {t^*}_2 \\ \Delta {t^*}_3 \\ \vdots \\ \Delta {t^*}_d \end{bmatrix} \tag{4.8}$$

The design matrix, $\mathbf{A}$, is the raypath intersection with the model multiplied by the slowness where l_{ij} is the length of ray path i in block j and s_j is the slowness in block j. $\mathbf{b}$ is equal to the difference between the predicted t^* and the observed t^*. The background attenuation model (see below for discussion) was multiplied by $\mathbf{A}$ to obtain the predicted t^*. $\mathbf{x}$ is the Q_p^{-1} perturbations from the background model.

A 2D Laplacian regularization multiplied by a damping parameter was applied to minimize curvature between nearby blocks and overcome noise levels. Several damping parameters were tested to find the minimization of the residual norm and model length.

Ray paths were weighted by SNR and t^* residual RMS. t^* were averaged for rays that follow the same path so that clusters of earthquakes did not bias the inversion result.

Including regularization and weighting, Equation 4.7 becomes

$$\begin{bmatrix} \mathbf{W}\ \mathbf{A} \\ \lambda\mathbf{\Theta} \end{bmatrix} \mathbf{x} = \begin{bmatrix} \mathbf{W}\ \mathbf{b} \\ \mathbf{0} \end{bmatrix} \tag{4.9}$$

where λ is the damping parameter, $\mathbf{\Theta}$ is the regularization matrix, and $\mathbf{W}$ is the weighting matrix. LSQR was used to solve this inversion problem to obtain the Q_p^{-1} perturbations [*Paige and Saunders*, 1982]. Negative Q_p^{-1} values were not allowed since negative attenuation is physically unrealistic. This a priori constraint was included in the iteration algorithm in LSQR (see *Herman* [1980]).

The following parameters needed to be determined before selecting the final model: condition limit, iteration limit, background model, and damping parameter.

Condition Limit

The condition number is the ratio of the largest and smallest eigenvalues of a matrix. When the small eigenvalue approaches 0, the condition number grows rapidly and the system becomes ill-conditioned. This is common in seismic tomography inversions. LSQR regulates the condition number through the parameter CONLIM. In an ill-conditioned system, the perturbation values may converge to a solution, but can grow rapidly without a stopping parameter. Thus, limiting the condition number and/or number of iterations is important for determining the optimum solution. Figure 4.13 shows that residual reduction occurs when $CONLIM \geq 10^6$. Previous studies suggest an ideal CONLIM value of $\frac{1}{10\sqrt{REPLR}}$ for ill-conditioned systems. REPLR is the precision of the machine floating point arithmetic. In this case, the ideal CONLIM is $6.71 \cdot 10^6$ which was used in the final inversion.

Iteration Limit

ITNLIM is an input parameter that limits the iteration number. LSQR will continue to iterate until a different stopping parameter if not given an iteration limit. Several inversions with varying iteration limits were tested. Figure 4.14 shows the iteration limit versus residual norm of each inversion. Residuals are reduced by iteration 100. Figure 4.15 shows the residual reduction and model length trade-off for the various iteration limits. ITNLIM equal to 50 optimizes residual norm and model length. However, we selected ITNLIM equal to 100 in order to obtain the smallest significant residual reduction while also limiting the model length.

Background Model

Tomography results are often dependent on the background model. In body-wave tomography, variations in 1D model can result in varying anomaly patterns and absolute velocities. *Tepp et al.* [2014] found that the 1-D model presented in Figure 4.2 was optimal. In some cases, 1-D velocity models are derived from geophysical surveys (i.e. refraction, gravity). A 1-D attenuation model beneath Sierra Negra does not exist. Therefore, we searched for an optimal 1-D background model by running a series of single iteration inversion with varying Q_p background (Figure 4.16). $Q_p = 150$ minimized the model residuals.

A single iteration with background $Q_p = 150$ was run and the mean Q_p for each layer was determined. The mean Q_p of each layer was used as the new background model for that layer in the following iteration. This process is repeated until the mean layer Q_p does not change significantly. This process produced mean Q_p similar to $Q_p = 150$ for all layers. Therefore, a homogeneous background attenuation of $Qp = 150$ was used in the final inversion.

Damping Parameter

Several inversions for a sequence of damping parameters were determined using the condition limit, iteration limit, and background model described above. The trade-off between model length and residual norm was used to determine the optimal damping parameter. Figure 4.17 shows the L-curve for the various inversions. The models did not vary significantly for λ ranging from $0.1 - 5$. In this range, $\lambda = 0.75$ optimized the model length and residual norm. Therefore, it was used in the final inversion.

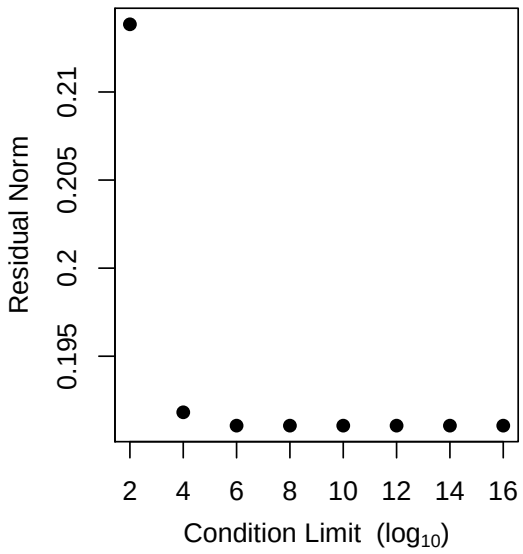

Figure 4.13: Residual norm of inversions as a function of condition limit.

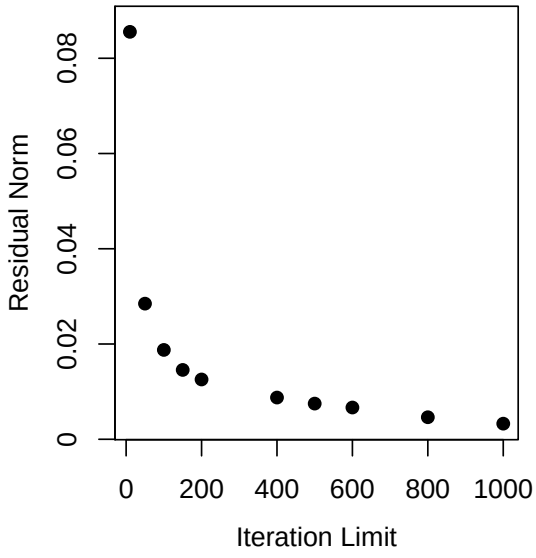

Figure 4.14: Residual norm of inversions with varying iteration limits. Residuals are reduced after 200 iterations.

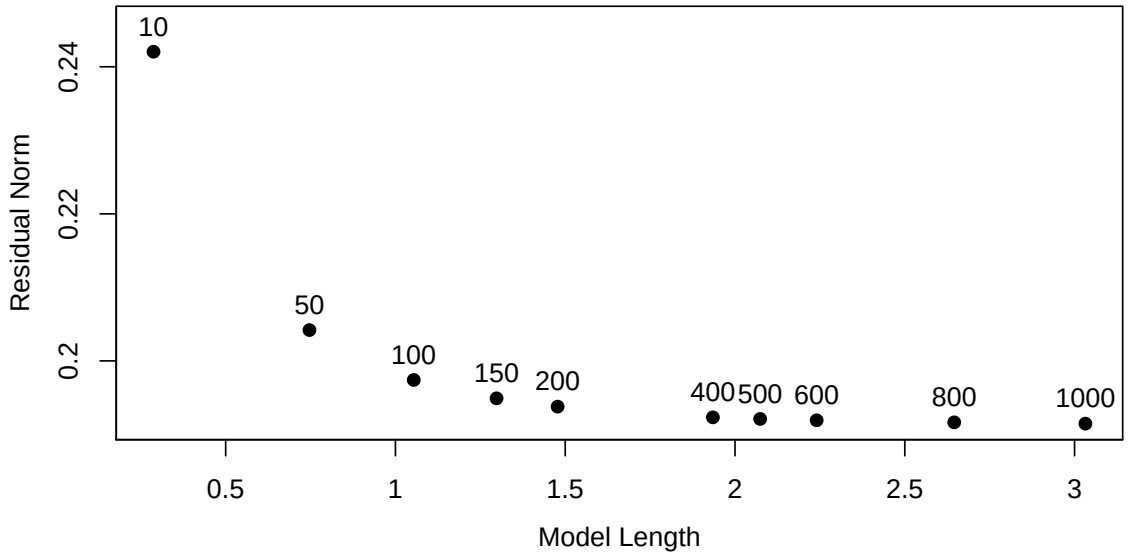

Figure 4.15: Model length versus residual norm for several inversions with varying iteration limits. 50 iterations minimizes residual norm and model length.

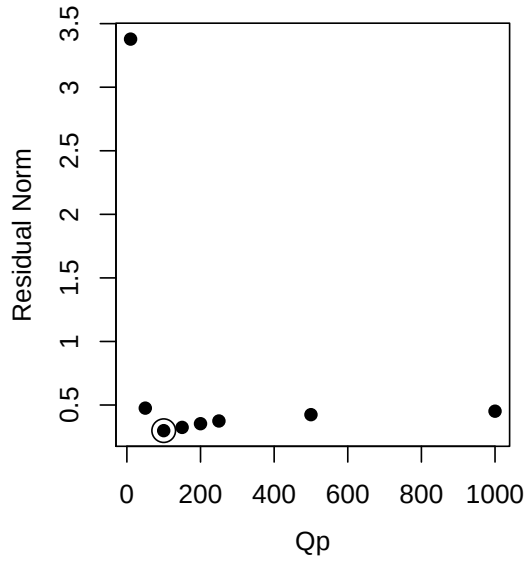

Figure 4.16: Background Q_p, plotted by residual norm from single-iteration inversions. Residual norm is minimized for $Q_p = 150$.

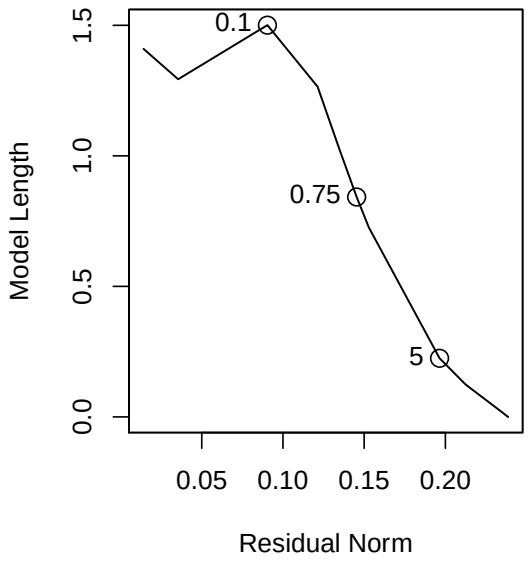

Figure 4.17: Trade-off curve of residual norm and model length for various damping parameters. $\lambda = 0.75$ was selected because larger values resulted in too smooth of model.

4.4 Synthetic Resolution Testing

Before interpretting a tomography model, resolution must be considered. The resolution is limited by the frequency of the seismic signals and ray coverage [*Lees*, 2007]. When ray coverage is homogeneous and dense, resolution is good. Two methods were used to estimate the model resolution: spike and checkerboard tests.

4.4.1 Spike Test

For the spike test, a $Q_p^{-1} = 0.03$ perturbation is added to a single block in a homogeneous near-zero background attenuation. Synthetic t^* were computed through the perturbed model and inverted to recover the perturbed spike. When resolution is perfect, the recovered spike will be the same as the input spike. As resolution decreases the information will be smeared into surrounding blocks.

Spike tests were calculated and used to estimate resolution at various key points in the model (Table 4.3; points in Figure 4.23b). Figure 4.18 shows one spike test result. The left panel displays the recovered spike in 2-D. The resolution in the X- and Y- directions was determined by measuring the number of blocks away frin tge block with the spike that are perturbed multipled by 0.5 km. The right panel displays the same result in 3-D, where the Z-axis and color correspond to the recovered Q_p^{-1}. The spike is narrow indicating that resolution is good in this block. Results indicate that resolution is best within the caldera, particularly at shallower depths. Resolution outside the caldera varies widely from $1 - 7$ km. Recovery of spikes is poor, never exceeding 10% (Table 4.3).

4.4.2 Checkerboard Tests

Several checkerboard patterns with varying dimensions of high and low perturbations were created. Synthetic t^* were computed through the perturbed models and inverted to reover the Q_p^{-1} checkerboard model (Figures 4.19−4.21). A second set of checkerboard tests were run with random noise added to the synthetic data prior to the inversion

(Figure 4.22). Addition of noise does not significantly affect the recovered checkerboard pattern, but recovery of the perturbed magnitudes is reduced at deeper depths.

Fine-scale (3 km) (Figure 4.19) and large-scale (6 km) (Figure 4.20) structures are resolveable beneath and east of caldera from $0.5 - 8$ km depths. Resolution and recovery decrease at depths > 8 km. Despite poor resolution and significant smearing, high and low attenuation is observable down to 13 km depth. Depths > 13 km are not resolveable and are not included in the results.

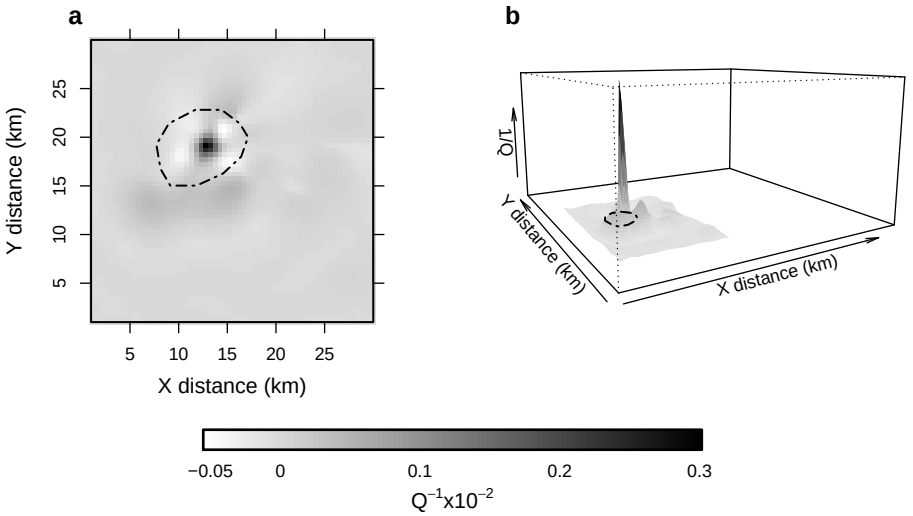

Figure 4.18: Spike test recovery results of point 1 in layer 2 ($0.5 - 3$ km) shown in (a) 2D X-Y plot and (b) 3D plot with Z-axis corresponding to recovered Q_p^{-1}

Table 4.3: Resolution and recovery from point-spread functions for key points shown and labeled in Figure 4.23

Depth	Label	X (km)	Y (km)	X-Res (km)	Y-Res (km)
0.5-3	1	12.3	19.1	2	2
0.5-3	2	13.9	21.6	1.5	2
0.5-3	3	17.8	21.6	7	6
0.5-3	4	17.7	16.4	3.5	3.5
0.5-3	5	11.6	16.0	3.5	6
3-5.5	1	12.7	25.0	6.5	8
3-5.5	2	11.0	20.0	4	4.5
3-5.5	3	10.1	16.2	4.5	7
3-5.5	4	16.6	15.9	9	6
3-5.5	5	21.0	15.6	4.5	7
3-5.5	6	24.6	19.1	16	3
3-5.5	7	19.2	20.4	6	5.5
5.5-8	1	12.6	19.3	2.5	2.5
5.5-8	2	12.3	22.7	3	3.5
5.5-8	3	16.5	19.9	3.5	3
5.5-8	4	20.5	11.6	4.5	5.5
8-10.5	1	16.4	20.2	6.5	4
8-10.5	2	20.2	11.8	4	5.5
8-10.5	3	11.9	12.1	6	5.5
8-10.5	4	11.3	17.3	7	8
10.5-13	1	14.9	14.2	6.5	6
10.5-13	2	16.5	4.7	5.5	8

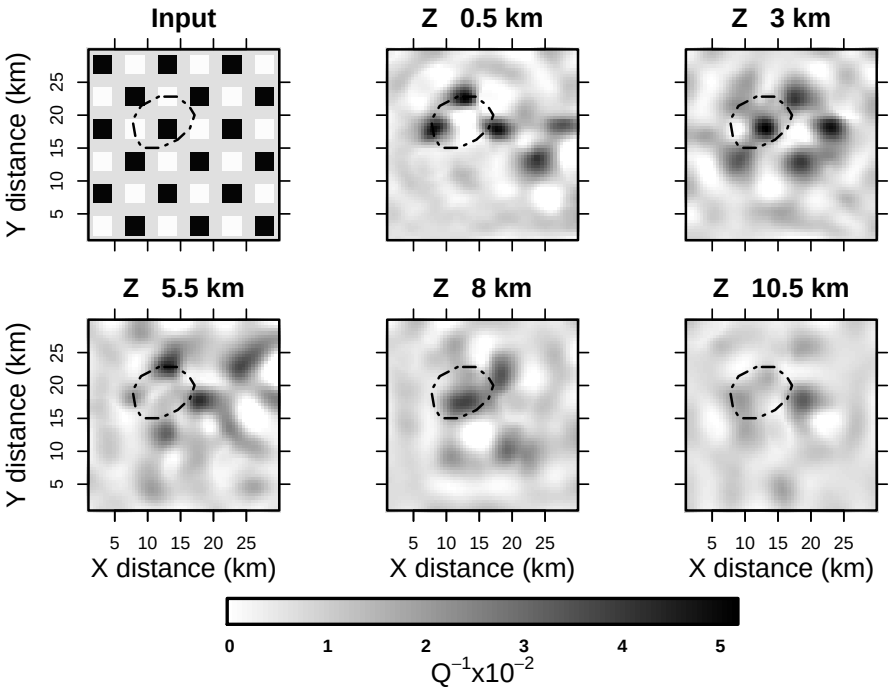

Figure 4.19: The input panel shows 3 x 3 km checkerboard perturbations with input of 0.05, 0.001, and 0.0067 for high, low, and background Q_p^{-1} respectively. The checkers alternate for each layer. Odd layers are the same as shown in the Input panel. Even layers, checkers alternate (i.e. black becomes white and vice versa). Synthetic t^* were calculated through the perturbed model. Inversion results are presented in the depth panels. Z corresponds to the depth for each panel. Caldera is shown by dashed ellipse.

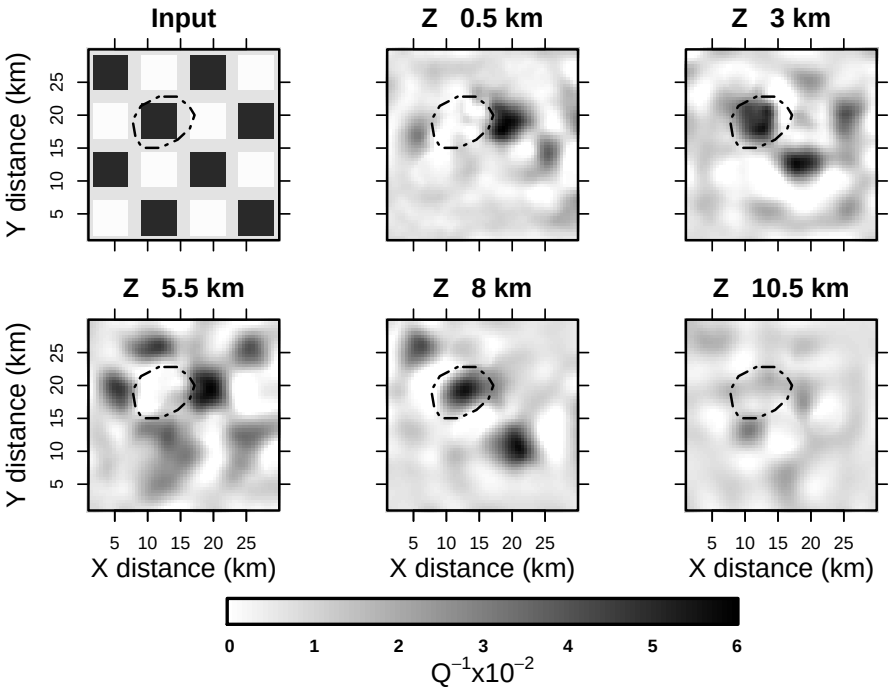

Figure 4.20: The input panel shows 6 x 6 km checkerboard perturbations with input of 0.05, 0.001, and 0.0067 for high, low, and background Q_p^{-1} respectively. The checkers alternate for each layer. Odd layers are the same as shown in the Input panel. Even layers, checkers alternate (i.e. black becomes white and vice versa). Synthetic t^* were calculated through the perturbed model. Inversion results are presented in the depth panels. Z corresponds to the depth for each panel. Caldera is shown by dashed ellipse.

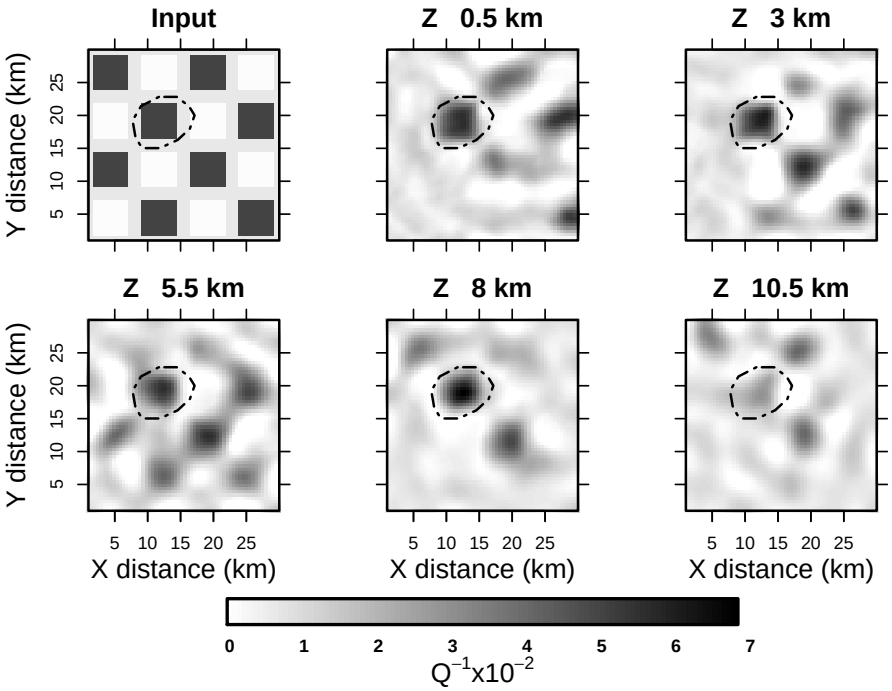

Figure 4.21: The input panel shows 6 x 6 km checkerboard perturbations with input of 0.05, 0.001, and 0.0067 for high, low, and background Q_p^{-1} respectively. The checkers do not alternate by layer. Synthetic t^* were calculated through the perturbed model. Inversion results are presented in the depth panels. Z corresponds to the depth for each panel. Caldera is shown by dashed ellipse.

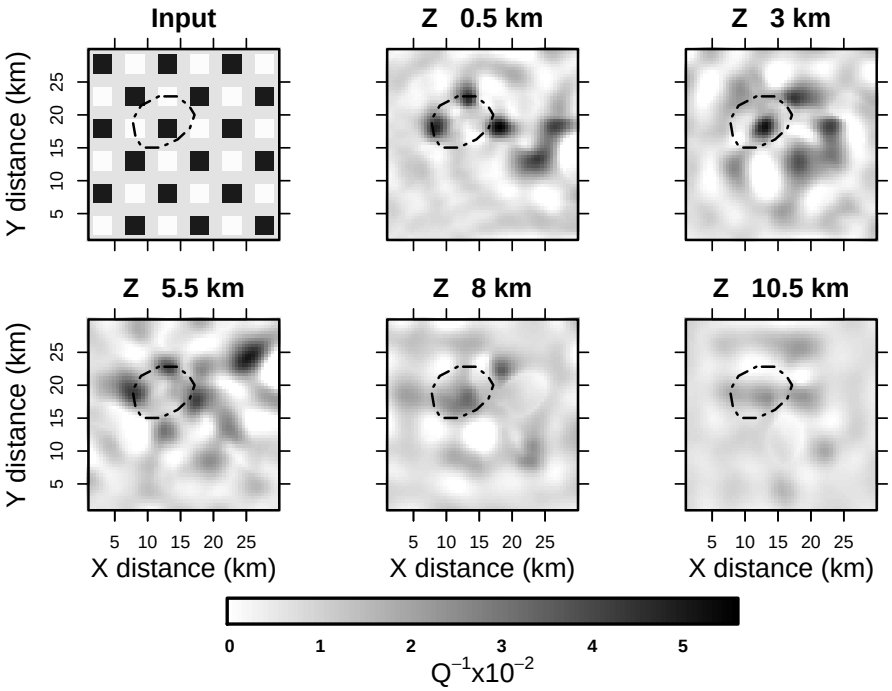

Figure 4.22: The input panel shows 3 x 3 km checkerboard perturbations with input of 0.05, 0.001, and 0.0067 for high, low, and background Q_p^{-1} respectively. The checkers alternate for each layer. Odd layers are the same as shown in the Input panel. Even layers, checkers alternate (i.e. black becomes white and vice versa). Synthetic t^* were calculated through the perturbed model. Random noise is added to the synthetic t^* and inverted. Inversion results are presented in the depth panels. Z corresponds to the depth for each panel. Caldera is shown by dashed ellipse.

4.5 Results

Results from the final tomographic inversion and the V_p model [*Tepp et al.*, 2014] are plotted in 5 panels corresponding to different depth layers in Figure 4.23a-b. Anomalies in areas of poor resolution (outlined by a thin line in Figure 4.23b) are not described. High and low attenuation are considered $Q_p^{-1} > 0.01$ and $Q_p^{-1} < 0.005$, respectively.

High attenuation is concentrated beneath the caldera from $0 - 10.5$ km depth. This zone is partially continuous, although there are significant spatial and magnitude variations in Q_p^{-1}. From $0 - 3$ km depth, there is high attenuation ranging from $0.01 - 0.04$ directly beneath the caldera (Anomaly A). This correlates with low V_p [*Tepp et al.*, 2014] and low group velocity [*Seats et al., in prep*, 2016]. West of the caldera, there is a small high attenuation (~ 0.01) circular zone. From $3 - 5.5$ km depth, high attenuation (~ 0.02) is concentrated in the northern caldera (Anomaly B). There is low V_p anomaly at this depth, but it is further north than Anomaly B. There is a high attenuation linear anomaly with $Q_p^{-1} \sim 0.01$ south of the caldera at this depth as well (Anomaly C). It is evident in cross-section that Anomaly B deepens southward and decreases in attenuation from $5.5 - 10.5$ km depth (Figure 4.23c-e).

Low attenuation anomalies (Anomaly D) surround the high attenuation zones. From $3 - 5.5$ km depth, Anomaly D is concentrated beneath and east of the caldera. From $5.5 - 8$ km depth, Anomaly D is present east, south, and west of the caldera. From $8 - 10.5$ km depth, low attenuation is primarily concentrated southeast of the caldera. There are no significant attenuation anomalies below 10.5 km depth.

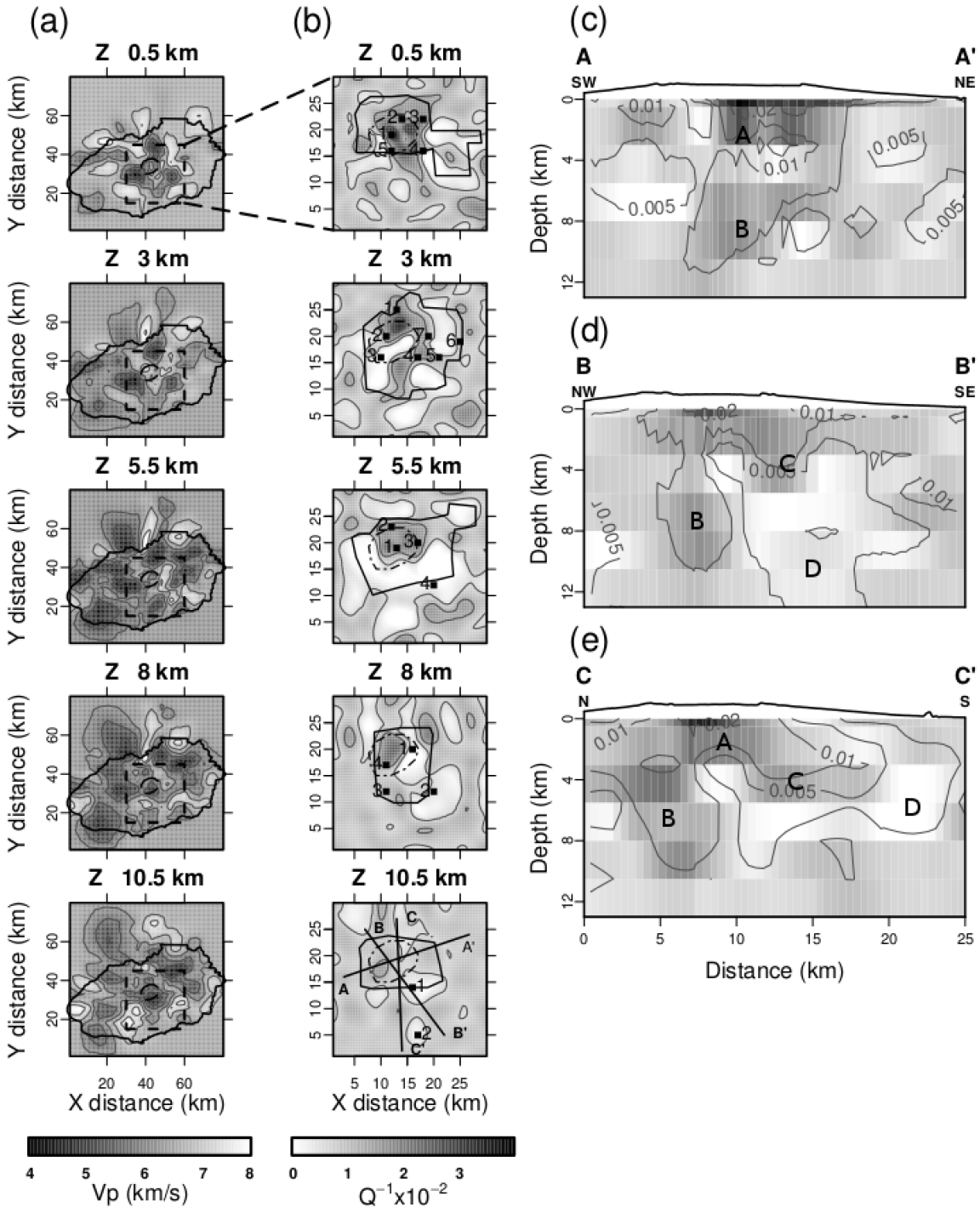

Figure 4.23: Model of (a) V_p derived from body-wave tomography [*Tepp et al.*, 2014] and (b) Q_p^{-1} shown in 5 panels corresponding to varying depth layers. The dashed box in (a) outlines the grid boundaries of the Q_p^{-1} results. Labeled points in (b) correspond to spike test points in Table S1. Resolveable regions are outlined by black polygons. Solid lines in Figure (b), panel 5 correspond to the vertical cross-sections shown in (c-e). Contours correpond to Q_p^{-1} equal to 0.005, 0.01, 0.02, and 0.04.

4.6 Model Uncertainty

4.6.1 Variance of Q_p^{-1}

A jackknife statistical test was used to estimate the uncertainty of the Q_p^{-1} model following a similar approach as *Lees and Lindley* [1994]. Jackknifing is a sub sampling technique used to determine the influence that observations have on the model. Data is randomized and separated into 75 non-overlapping sets. Statistical summaries of inversions derived for each set of data are used to estimate the variance of the model parameters. The variance of Q_p^{-1} for each block (i.e. grid point) in Figure 4.23 is shown in Figure 4.24. Variances range from $0 - 0.008$. In blocks with zero coverage, the variance is zero. Blocks with good coverage have the smallest errors. At depths < 0.5 km, the largest error is concentrated beneath stations where ray paths converge. Other large errors are concentrated in regions with low coverage and/or near blocks with zero coverage. The mean variance, excluding blocks with zero coverage, is 0.0005. This is low relative to the resolved Q_p^{-1} model indicating the Q_p^{-1} model has small error.

4.6.2 Probability of Randomness

In high-scattering regimes, loss of t^* signal coherence can occur [*De Siena et al.*, 2010]. Volcanic cones tend to be highly heterogeneous resulting in a high-scattering regime. Therefore, loss of signal coherence is a concern in the study area. If signal coherence is lost, t^* determinations will not be spatially correlated and will appear random. Monte Carlo simulations were used to calculate the probability that the observed Q_p^{-1} model parameters are a result of random t^*. Synthetic random data sets of length, mean, and standard deviation equal to the observed t^* were inverted to produce 10000 synthetic models. For each block, the number of synthetic Q_p^{-1} values that lie between the observed $Q_p^{-1} \pm$ variance is divided by the number of simulations to determine the probability of randomness (Figure 4.25). Blocks with zero coverage have 0% randomness since the variance is also zero (see previous section). Above 0.5 km, randomness is large especially

beneath the caldera. Randomness is low at depths > 0.5 km. Therefore, it is unlikely that Q_p^{-1} observations beneath the caldera (> 0.5 km) were produced by random noise.

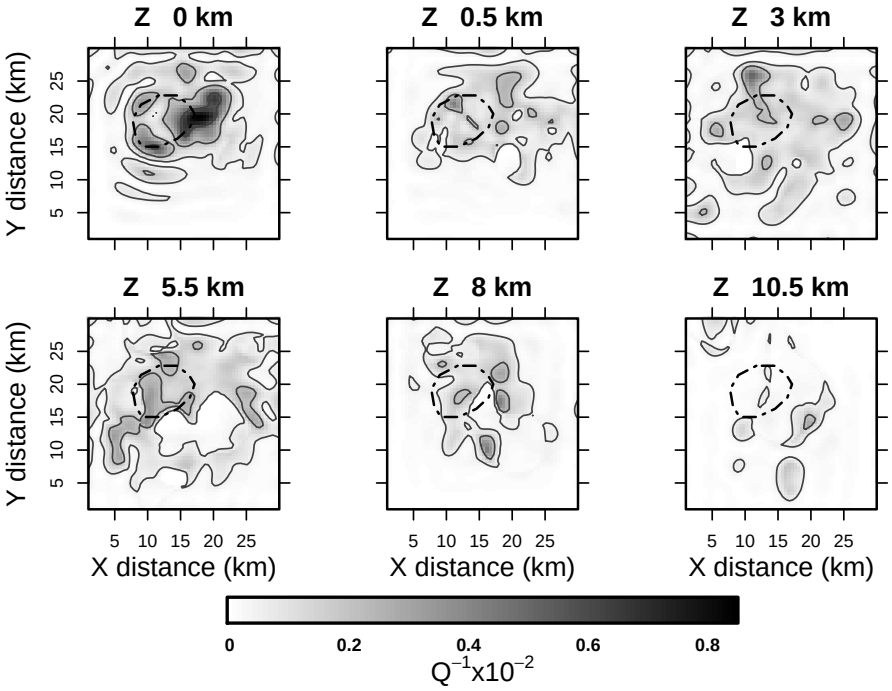

Figure 4.24: Variance of grid points in Q_p^{-1} model (Figure 3) derived from a jackknife statistical test. Z corresponds to the depth for each panel. Caldera is shown by dashed black ellipse.

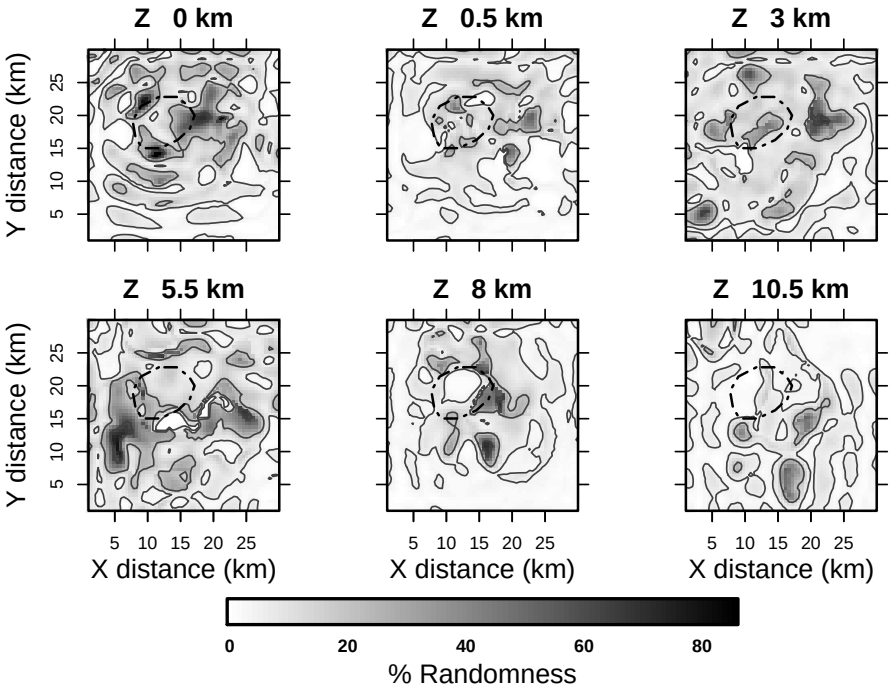

Figure 4.25: Probability of randomness derived from 10000 Monte Carlo simulations. Z corresponds to the depth for each panel. For each grid point, the percentage of points within the observed $Q_p^{-1} \pm \sigma^2$ is used to estimate the probability of randomness. Large percentages suggest artifical Q_p^{-1}. Thus, regions with large % should not be interpretted.

Table 4.4: Variance and probability of randomness for key points as labeled in Figure 4.23

Depth	Label	X (km)	Y (km)	σ^2 ($Q_p^{-1} \cdot 10^{-4}$)	% Random
0.5-3	1	12.3	19.1	1.4	2.7
0.5-3	2	13.9	21.6	2.0	6.9
0.5-3	3	17.8	21.6	2.4	9.0
0.5-3	4	17.7	16.4	1.4	4.1
0.5-3	5	11.6	16.0	0.5	3.2
3-5.5	1	12.7	25.0	1.9	5.9
3-5.5	2	11.0	20.0	1.5	4.3
3-5.5	3	10.1	16.2	2.5	9.1
3-5.5	4	16.6	15.9	9.2	13.4
3-5.5	5	21.0	15.6	3.3	5.7
3-5.5	6	24.6	19.1	0	0
3-5.5	7	19.2	20.4	15.0	14.7
5.5-8	1	12.6	19.3	7.0	13.8
5.5-8	2	12.3	22.7	14.7	22.4
5.5-8	3	16.5	19.9	8.7	20.2
5.5-8	4	20.5	11.6	11.2	37.1
8-10.5	1	16.4	20.2	3.6	5.3
8-10.5	2	20.2	11.8	1.8	8.5
8-10.5	3	11.9	12.1	0.5	2.4
8-10.5	4	11.3	17.3	0.9	4.3
10.5-13	1	14.9	14.2	3.0	8.5
10.5-13	2	16.5	4.7	0.2	1.9

4.7 Discussion

High Q_p^{-1} is most commonly attributed to magma accumulation, temperature gradients, fluid presence, magma movement, and heterogeneous media in volcanic settings [*Lees*, 2007]. Q_p^{-1} should be studied in conjunction with V_p, V_s, Q_s^{-1}, and g, the scattering coefficient, to differentiate the causes of attenuation. Currently, only V_p and U_g models of Sierra Negra exist [*Tepp et al.*, 2014, ;*Seats et al., in prep*, 2016;]. Thus, our interpretation of the attenuation structure and understanding of the magmatic system is limited.

Attenuation is greatest at shallow depths (< 0.5 km) beneath the caldera. Near-surface attenuation is often attributed to fluid presence and high-scattering regime in volcanic tomography studies. Several Galápagos volcanoes have known perched aquifer systems [*Violette et al.*, 2014]. If Sierra Negra has a similar system, this could explain the high Q_p^{-1} signal. The shallow attenuation could also be caused by scattering due to successive volcanic extrusions. Monte Carlo simulations strongly suggest lack of signal coherence at depths < 0.5 km which likely resulted from heterogeneity in the shallow subsurface. When discussing attenuation structures, these depths are not considered.

Attenuation tends to incrementally decrease with depth until 10.5 km. This trend is expected due to increased confining pressure. Poorer magnitude recovery at depths > 5.5 km could also produce this trend (Table S1, Figures S2-S5). Anomalies A and B are the two dominant high attenuation anomalies. Anomaly A is concentrated beneath the caldera, while Anomaly B is centered in the northern caldera and deepens southward. The spatial variation suggests these regions could be separate attenuating bodies. However, the relative uniformity in Q_p^{-1} suggests that the rock properties and thermal state of the system are similar in the regions.

4.7.1 Temperature Estimates from Q_p^{-1}

Laboratory experiments indicate a strong temperature dependence of Q^{-1}. At high temperatures, Q^{-1} follows the power law

$$Q^{-1} \sim f^{-\alpha} e^{\frac{-A'}{RT}} \tag{4.10}$$

with $\alpha = 0.15 - 0.3$ and and $A' = 100 - 200 \frac{kJ}{mol}$. The proportion coefficient and α in Equation 4.10 depend on the rock composition. For example, increasing pyroxene content increases the absorption [*Kampfmann and Berckhemer*, 1985]. For a dunite, $Q^{-1} = 3 \cdot 10^5 f^{-0.28} e^{\frac{-195}{RT}}$, while for a peridotite, $Q^{-1} = 5.3 \cdot 10^4 f^{-0.28} e^{\frac{-163}{RT}}$. More recent studies characterize the influence of porosity and grain-size on Q^{-1} and temperature estimates [*Faul and Jackson*, 2005; *Jackson and Faul*, 2010].

Given an average Q_p^{-1} of 0.01, the temperature is estimated at $1050 - 1100\ ^\circ C$ [*Kampfmann and Berckhemer*, 1985; *Faul and Jackson*, 2005; *Jackson and Faul*, 2010]. For pockets of largest Q_p^{-1} ($\sim 0.02 - 0.03$) at 0.5 and 3 km depths, temperature is estimated at 1150 $^\circ C$. This is consistent with *Geist et al.* [2008] melt temperature calculation of 1128 $^\circ C$ determined by thermobarometry of the 2005 extrusion. Given similar Q_p^{-1} and frequency, grain-size or presence of fluid (see *Jackson and Faul* [2010]) does not alter the temperature estimates by $> 50\ ^\circ C$. Note that the temperature estimates are based on olivine-rich mafic rock compositions (i.e. mantle rock). Given the ocean-island volcanism source, magma is expected to less mafic than a mantle source. Thus, temperature estimates may be underestimated. Furthermore, this assumes that the attenuation is only thermally-induced and this may not be the case. The temperature estimates only provide a sense of the temperature in the study region. Until crustal and/or volcanic experimental attenuation studies are done, we can not say with any certainty the temperature.

There is a significant low U_g signature for 2 s and 3 s periods which could translate to low V_s at shallow depths. It is possible that the the highest Q_p^{-1} signatures (0 and

3 km depth) are due to partial melting or fluid presence, not increased temperatures. Correlations between V_s and Q^{-1} in tomography studies suggest Q^{-1} is also dependent on melt %, although this is not yet quantified [*Hammond and Humphreys*, 2000]. Without a V_s model, we can only speculate that partial melting may contribute to the observed high attenuation signals.

4.7.2 Magma Accumulation Zones

We interpret the high attenuation anomalies as zones of magma accumulation beneath the caldera. The top of the magma zone ($0.5 - 3$ km depth) is consistent with the 2.1 km determination from deformation modeling [*Amelung et al.*, 2000; *Geist et al.*, 2006; *Yun et al.*, 2006]. The top of this zone extends northeast and southeast of the caldera rim. Monte Carlo testing indicates the southeastern signal is artificial. The northeastern region is resolvable and real, but smearing is significant. Accounting for poor resolution and smearing, the diameter extends 2 km beyond the caldera rim and generally decreases with depth. Resolution is poor below 10.5 km, but a high Q_p^{-1} anomaly is still visible in checkerboard testing. Given the absence of observed high Q_p^{-1} at this depth, we suggest 10.5 km is the greatest extent of shallow magma accumulation. Given a 2.1 km top, the volume of the magma accumulation zones is $\sim 3 \cdot 10^{11}$ m^3. This is likely an overestimation due to smearing effects.

Low attenuation zones surround Anomaly B and roughly correlate with a high V_p anomaly from $5.5-10.5$ km depth. In volcanic settings, low attenuation and high velocity are mostly commonly attributed to cooled lava rock with limited fluid presence [*Lees*, 2007]. Compositional differences could also produce such a signal. We interpret the low attenuation as cooled lava rock at the sides and base of the magma accumulation zone.

4.7.3 Comparison to previous models

Caldera deformation modeling indicates a sill or flat-topped diapir at 2.1 km depth relative to the caldera floor [*Amelung et al.*, 2000; *Geist et al.*, 2006; *Yun et al.*, 2006]. For a caldera with a large radius relative to depth, only the geometry of the upper portion of the chamber controls deformation. Thus, a thin sill or flat-topped diapir explain the observed deformation equally well [*Yun et al.*, 2006]. However, dike and sill orientations favor the diapir model [*Chadwick and Dieterick*, 1995].

If Anomalies A and B are considered two different zones of magma accumulation, this would suggest at least two stacked reservoirs: one shallow sill between $0.5 - 3$ km depth controlling surface deformation and a deeper magma zone from $3 - 10.5$ km depth. However, there is not strong evidence to indicate the anomalies are different since they overlap spatially and have similar Q_p^{-1} signatures. Finer vertical grid spacing is required to confirm a multiple chamber geometry. Thus, we suggest there is continuous magma accumulation zone with local Q_p^{-1} variations beneath Sierra Negra. This interpretation supports the diapir model.

Our model suggests a much smaller magma region than proposed by *Tepp et al.* [2014]. Body-wave tomography imaged a large low V_p zone from $5.5 - 15$ km depth interpreted as a possible zone of magma accumulation [*Tepp et al.*, 2014]. It is possible that the high attenuation zone correlates with a volumetrically smaller and lower V_p pocket within the large low V_p anomaly as described in *Tepp et al.* [2014]. Differences in methodology and scale could also account for the discrepancy in size and depth of magma accumulation. Similar size differences between attenuation and velocity models have been observed in other volcano tomography studies [e.g. *Prudencio et al.*, 2015].

This study could not resolve a conduit system or deeper magma storage beneath the diapir. *Villagomez et al.* [2014] suggests that a low V_s anomaly between the crust and 80 km depth beneath the Galápagos drives volcanism at Sierra Negra, Cerro Azul, and Fernandina. Further imaging below 15 km depth is necessary to resolve the conduit

structure between the shallow reservoir beneath Sierra Negra and the larger magma storage zones.

4.8 Conclusion

Spectral decay method was used to determine the Q_p^{-1} structure beneath Sierra Negra. High attenuation is concentrated beneath the caldera from $0.5 - 10.5$ km depth that is interpreted as a zone of magma accumulation. Further attenuation studies modeling Q_s^{-1} and g could distinguish the sources of high attenuation. Our results favor the diapir model of caldera deformation with a flat-top at 2.1 km as described in *Yun et al.* [2006]. The conduit system between the diapir and deeper storage zone is unexplored and should be a target for future study to gain a fuller understanding of the magma system at Sierra Negra.

REFERENCES

Abercrombie, R. (1995), Earthquake source scaling relationships from -1 to 5 M(L) using seismograms recorded at 2.5-km depth, *J. Geophys. Res.*, *100*(B12), 24,015–24,036, doi:10.1029/95JB02397.

Aki, K. (1969), Use of Coda Waves for Study of Microearthquake Source Mechanism, *T. Am. Geophys. Un.*, *50*(5), 404–&.

Aki, K. (1980), Scattering and Attenuation of Shear-waves in the Lithosphere, *J. Geophys. Res.*, *85*(NB11), 6496–6504, doi:10.1029/JB085iB11p06496.

Aki, K., and B. Chouet (1975), Origin of Coda Waves - Source, Attenuation, and Scattering Effects, *J. Geophys. Res.*, *80*(23), 3322–3342, doi:10.1029/JB080i023p03322.

Aki, K., and P. Richards (2002), *Quantitative Seismology*, University Science Books.

Amelung, F., S. Jonsson, H. Zebker, and P. Segall (2000), Widespread uplift and 'trapdoor' faulting on Galapagos volcanoes observed with radar interferometry, *Nature*, *407*(6807), 993–996.

Bellis, C., and B. Holtzman (2014), Sensitivity of seismic measurements to frequency-dependent attenuation and upper mantle structure: An initial approach, *J. Geophys. Res*, *119*(7), 5497–5517, doi:10.1002/2013JB010831.

Bennington, N., C. Thurber, and S. Roecker (2008), Three-Dimensional Seismic Attenuation Structure around the SAFOD Site, Parkfield, California, *B. Seismol. Soc. Am.*, *98*(6), 2934–2947, doi:10.1785/0120080175.

Berckhemer, H., W. Kampfmann, E. Aulback, and H. Schmeling (1982), Shear Modulus and Q of Forsterite and Dunite Near Partial Melting from Forced-Oscillation Experiemnts, *Phys. Earth Planet. In.*, *29*(1), 30–41, doi:10.1016/0031-9201(82)90135-2.

Boatwright, J. (1978), Detailed spectral analysis of 2 small New-York-State earthquakes, *B. Seismol. Soc. Am.*, *68*(4), 1117–1131.

Brune, J. (1970), Tectonic stress and spectra of seismic shear waves from earthquakes, *J. Geophys. Res*, *75*(26), 4997–&, doi:10.1029/JB075i026p04997.

Calvet, M., and L. Margerin (2013), Lapse-Time Dependence of Coda Q: Anisotropic Multiple-Scattering Models and Application to the Pyrenees, *B. Seismol. Soc. Am.*, *103*(3), 1993–2010, doi:10.1785/0120120239.

Chadwick, W., and J. Dieterick (1995), Mechanical Modeling of Circumferential and Radial Dike Intrustion on Galapagos Volcanos, *J. Volcanol. Geoth. Res.*, *66*(1-4), 37–52, doi:10.1016/0377-0273(94)00060-T.

Chadwick, W. W., Jr., D. J. Geist, S. Jonsson, M. Poland, D. J. Johnson, and C. M. Meertens (2006), A volcano bursting at the seams: Inflation, faulting, and eruption at Sierra Negra volcano, Galapagos, *Geology*, *34*(12), 1025–1028, doi:10.1130/G22826A.1.

De Lorenzo, S., A. Zollo, and G. Zito (2010), Source, attenuation, and site parameters of the 1997 Umbria-Marche seismic sequence from the inversion of P wave spectra: A comparison between constant Q(P) and frequency-dependent Q(P) models, *J. Geophys. Res*, *115*, doi:10.1029/2009JB007004.

De Siena, L., E. Del Pezzo, F. Bianco, and A. Tramelli (2009), Multiple resolution seismic attenuation imaging at Mt. Vesuvius, *Phys. Earth Planet In.*, *173*(1-2), 17–32, doi: 10.1016/j.pepi.2008.10.015.

De Siena, L., E. Del Pezzo, and F. Bianco (2010), Seismic attenuation imaging of Campi Flegrei: Evidence of gas reservoirs, hydrothermal basins, and feeding systems, *J. Geophys. Res*, *115*, doi:10.1029/2009JB006938.

De Siena, L., E. Del Pezzo, C. Thomas, A. Curtis, and L. Margerin (2013), Seismic energy envelopes in volcanic media: in need of boundary conditions, *Geophys. J. Int.*, *195*(2), 1102–1119, doi:10.1093/gji/ggt273.

De Siena, L., C. Thomas, and R. Aster (2014a), Multi-scale reasonable attenuation tomography analysis (MuRAT): An imaging algorithm designed for volcanic regions, *J. Volcanol. Geoth. Res.*, *277*, 22–35, doi:10.1016/j.jvolgeores.2014.03.009.

De Siena, L., C. Thomas, G. P. Waite, S. C. Moran, and S. Klemme (2014b), Attenuation and scattering tomography of the deep plumbing system of Mount St. Helens, *J. Geophys. Res*, *119*(11), 8223–8238, doi:10.1002/2014JB011372.

Del Pezzo, E., F. Bianco, L. De Siena, and A. Zollo (2006), Small scale shallow attenuation structure at Mt. Vesuvius, Italy, *Phys. Earth Planet In.*, *157*(3-4), 257–268, doi:10.1016/j.pepi.2006.04.009.

Eberhart-Phillips, D., and M. Chadwick (2002), Three-dimensional attenuation model of the shallow Hikurangi subduction zone in the Raukumara Peninsula, New Zealand, *J. Geophys. Res*, *107*(B2), doi:10.1029/2000JB000046.

Eberhart-Phillips, D., M. Reyners, M. Chadwick, and J. Chiu (2005), Crustal heterogeneity and subduction processes: 3-D Vp, Vp/Vs and Q in the southern North Island, New Zealand, *Geophys. J. Int.*, *162*(1), 270–288, doi:10.1111/j.1365-246X.2005.02530.x.

Faul, U., and I. Jackson (2005), The seismological signature of temperature and grain size variations in the upper mantle, *Earth Planet. Sc. Lett.*, *234*(1-2), 119–134, doi: 10.1016/j.epsl.2005.02.008.

Geist, D., W. Chadwick, and D. Johnson (2006), Results from new {GPS} and gravity monitoring networks at fernandina and sierra negra volcanoes,

galpagos, 20002002, *J. Volcanol. Geoth. Res.*, *150*(13), 79 – 97, doi: http://dx.doi.org/10.1016/j.jvolgeores.2005.07.003, the Changing Shapes of Active Volcanoes Recent Results and Advances in Volcano Geodesy.

Geist, D., B. A. Diefenbach, D. J. Fornari, M. D. Kurz, K. Harpp, and J. Blusztajn (2008), Construction of the galpagos platform by large submarine volcanic terraces, *Geochem. Geophy. Geosy.*, *9*(3), n/a–n/a, doi:10.1029/2007GC001795.

Gibson, S., and D. Geist (2010), Geochemical and geophysical estimates of lithospheric thickness variation beneath galpagos, *Earth Planet. Sc. Lett.*, *300*(34), 275 – 286, doi:http://dx.doi.org/10.1016/j.epsl.2010.10.002.

Hammond, W., and E. Humphreys (2000), Upper mantle seismic wave attenuation: Effects of realistic partial melt distribution, *J. Geophys. Res*, *105*(B5), 10,987–10,999, doi:10.1029/2000JB900042.

Herman, G. T. (1980), *Image Reconstruction from Projections*, 193-196 pp., Academic Press.

Hough, S., J. Lees, and F. Monastero (1999), Attenuation and source properties at the Coso geothermal area, California, *B. Seismol. Soc. Am.*, *89*(6), 1606–1619.

Jackson, I. (1993), Progress in the experimental-study of seismic-wave attenuation, *Annu. Rev. Earth Pl. Sc.*, *21*, 375–406, doi:10.1146/annurev.earth.21.1.375.

Jackson, I., and U. H. Faul (2010), Grainsize-sensitive viscoelastic relaxation in olivine: Towards a robust laboratory-based model for seismological application, *Phys. Earth Planet In.*, *183*(1-2, SI), 151–163, doi:10.1016/j.pepi.2010.09.005.

Jackson, I., J. Fitz Gerald, U. Faul, and B. Tan (2002), Grain-size-sensitive seismic wave attenuation in polycrystalline olivine, *J. Geophys. Res.*, *107*(B12), doi: 10.1029/2001JB001225.

Jackson, I., U. Faul, J. Gerald, and B. Tan (2004), Shear wave attenuation and dispersion in melt-bearing olivine polycrystals: 1. Specimen fabrication and mechanical testing, *J. Geophys. Res*, *109*(B6), doi:10.1029/2003JB002406.

Jonsson, S., H. Zebker, and F. Amelung (2005), On trapdoor faulting at Sierra Negra volcano, Galapagos, *J. Volcanol. Geoth. Res.*, *144*(1-4), 59–71, doi: 10.1016/j.jvolgeores.2004.11.029.

Kampfmann, W., and H. Berckhemer (1985), High-temperature experiments on the elastic and anelastic behavior of magmatic rocks, *Phys. Earth Planet In.*, *40*(3), 223–247, doi:10.1016/0031-9201(85)90132-3.

Koulakov, I., S. El Khrepy, N. Al-Arifi, I. Sychev, and P. Kuznetsov (2014), Evidence of magma activation beneath the Harrat Lunayyir basaltic field (Saudi Arabia) from attenuation tomography, *J. Geophys. Res.*, *5*(2), 873–882, doi:10.5194/se-5-873-2014.

Lees, J., and G. Lindley (1994), 3-Dimensional Attenuation Tomogrpahy at Loma-Prieta - inversion of T-asterisk for Q, *J. Geophys. Res*, *99*(B4), 6843–6863, doi: 10.1029/93JB03460.

Lees, J. M. (2007), Seismic tomography of magmatic systems, *J. Volcanol. Geoth. Res.*, *167*(1-4), 37–56, doi:10.1016/j.jvolgeores.2007.06.008.

Lees, J. M. (2015a), *RSEIS: Seismic Time Series Analysis Tools*, r package version 3.5-2.

Lees, J. M. (2015b), *Rquake: Seismic Hypocenter Determination*, r package version 2.3-1.

Lees, J. M., and J. Park (1995), Multiple-taper spectral analysis: A stand-alone c-subroutine, *Comput. & Geosci.*, *21*(2), 199 – 236, doi:http://dx.doi.org/10.1016/0098-3004(94)00067-5, geophysics.

Lin, G., P. M. Shearer, F. Amelung, and P. G. Okubo (2015), Seismic tomography of compressional wave attenuation structure for Kilauea Volcano, Hawai"i, *J. Geophys. Res*, *120*(4), 2510–2524, doi:10.1002/2014JB011594.

Lindley, G., and R. Archuleta (1992), Earthquake source parameters and the frequency-dependence of attenuation at Coalinga, Mammoth Lakes, and the Santa-Cruz Mountains, California, *J. Geophys. Res*, *97*(B10), 14,137–14,154, doi:10.1029/92JB00550.

Liu, H., D. Anderson, and H. Kanamori (1976), Velocity Dispersion Due to Anelasticity - Implications for Seismology and Mantle Composition, *Geophys J, Roy. Astr. S.*, *47*(1), 41–58, doi:10.1111/j.1365-246X.1976.tb01261.x.

Nishigami, K. (1991), A New Inversion Method of Coda Wave-forms to Determine the Spatial-Distribution of Coda Scatterers in the Crust and Uppermost Mantle, *Geo. Res. Lett.*, *18*(12), 2225–2228, doi:10.1029/91GL02823.

Ohlendorf, S. J., C. H. Thurber, J. D. Pesicek, and S. G. Prejean (2014), Seismicity and seismic structure at Okmok Volcano, Alaska, *J. Volcanol. Geoth. Res.*, *278*, 103–119, doi:10.1016/j.jvolgeores.2014.04.002.

Paige, C., and M. Saunders (1982), LSQR-An algorithm for sparse linear-equations and sparse least-squares, *ACM T. Math. Software*, *8*(1), 43–71, doi:10.1145/355984.355989.

Prudencio, J., L. De Siena, J. M. Ibanez, E. Del Pezzo, A. Garcia-Yeguas, and A. Diaz-Moreno (2015), The 3D Attenuation Structure of Deception Island (Antarctica), *SURVEYS IN GEOPHYSICS*, *36*(3), 371–390, doi:10.1007/s10712-015-9322-6.

Randall, M. (1973), Spectral Theory of Seismic Sources, *Bull. Seismol. Soc. Am.*, *63*(3), 1133–1144.

Reynolds, R., D. Geist, and M. Kurz (1995), Physical Volcanology and structural development of Sierra Negra Volcano, Isabella Island, Galapagos Archipelago, *Geol. Soc. Am. Bull.*, *107*(12), 1398–1410, doi:10.1130/0016-7606(1995)107¡1398:PVASDO¿2.3.CO;2.

Rietbrock, A. (2001), P wave attenuation structure in the fault area of the 1995 Kobe earthquake, *J. Geophys. Res*, *106*(B3), 4141–4154, doi:10.1029/2000JB900234.

Rychert, C. A., N. Harmon, and C. Ebinger (2014), Receiver function imaging of lithospheric structure and the onset of melting beneath the Galapagos Archipelago, *Earth Planet. Sc. Lett.*, *388*, 156–165, doi:10.1016/j.epsl.2013.11.027.

Sarker, G., and G. Abers (1998), Deep structures along the boundary of a collisional belt: attenuation tomography of P and S waves in the Greater Caucasus, *Geophys. J. Int.*, *133*(2), 326–340, doi:10.1046/j.1365-246X.1998.00506.x.

Sato, H., and M. Fehler (2009), Seismic Wave Propagation and Scattering in the Heterogeneous Earth, in *Seismic Wave Propagation and Scattering in the Heterogeneous Earth*, Modern Acoustics and Signal Processing, pp. 1–308, doi:10.1007/978-3-540-89623-4.

Scherbaum, F. (1990), Combined inversion for the 3-dimensional Q-structure and source parameters using microearthquake spectra, *J. Geophys. Res*, *95*(B8), 12,423–12,438, doi:10.1029/JB095iB08p12423.

Shapiro, N., M. Campillo, L. Margerin, S. Singh, V. Kostoglodov, and J. Pacheco (2000), The energy partitioning and the diffusive character of the seismic coda, *Bull. Seismol. Soc. Am.*, *90*(3), 655–665, doi:10.1785/0119990021.

Shearer, P. (2009), *Introduction to Seismology*, Cambridge University Press.

Tepp, G., C. J. Ebinger, M. Ruiz, and M. Belachew (2014), Imaging rapidly deforming ocean island volcanoes in the western Galapagos archipelago, Ecuador, *J. Geophys. Res*, *119*(1), 442–463, doi:10.1002/2013JB010227.

Tramelli, A., E. Del Pezzo, F. Bianco, and E. Boschi (2006), 3D scattering image of the Campi Flegrei caldera (Southern Italy) - New hints on the position of the old caldera rim, *Phys. Earth Planet In.*, *155*(3-4), 269–280, doi:10.1016/j.pepi.2005.12.009.

Villagomez, D. R., D. R. Toomey, E. E. E. Hooft, and S. C. Solomon (2007), Upper mantle structure beneath the Galapagos Archipelago from surface wave tomography, *J. Geophys. Res*, *112*(B7), doi:10.1029/2006JB004672.

Villagomez, D. R., D. R. Toomey, D. J. Geist, E. E. E. Hooft, and S. C. Solomon (2014), Mantle flow and multistage melting beneath the Galapagos hotspot revealed by seismic imaging, *Nature Geoscience*, *7*(2), 151–156, doi:10.1038/NGEO2062.

Violette, S., N. d'Ozouville, A. Pryet, B. Deffontaines, J. Fortin, and M. Adelinet (2014), Hydrogeology of the Galapagos Archipelago: An Integrated and Comparative Approach Between Islands, in *Galapagos: A Natural Laboratory for the Earth Sciences*, *Geophysical Monograph Book Series*, vol. 204, edited by Harpp, KS and Mittelstaedt, E and DOzouville, N and Graham, DW, pp. 167–183.

Walsh, J. (1966), Seismic Wave Attenuaiton in Rock due to Friction, *J. Geophys. Res.*, *71*(10), 2591–&.

Warren, L., and P. Shearer (2000), Investigating the frequency dependence of mantle Q by stacking P and PP spectra, *J. Geophys. Res.*, *105*(B11), 25,391–25,402, doi: 10.1029/2000JB900283.

Winkler, K. W., and W. F. Murphy (1995), *Acoustic Velocity and Attenuation in Porous Rocks*, pp. 20–34, American Geophysical Union, doi:10.1029/RF003p0020.

Yoshimoto, K., H. Sato, and M. Ohtake (1993), Frequency-dependent attenuation of P-wave and S-wave in the Kanto Area, Japan, Based on the Coda-Normalization, *Geophys. J. Int.*, *114*(1), 165–174, doi:10.1111/j.1365-246X.1993.tb01476.x.

Yun, S., P. Segall, and H. Zebker (2006), Constraints on magma chamber geometry at Sierra Negra Volcano, Galapagos Islands, based on InSAR observations, *J. Volcanol. Geoth. Res.*, *150*(1-3), 232–243, doi:10.1016/j.jvolgeores.2005.07.009.